Deep banded orographic convection over an idealized mountain range: influence of upstream atmospheric conditions

Tullio Degiacomi[a], Andrea Zonato[a,b], Silvio Davolio[c,d], Mario Marcello Miglietta[e], Lorenzo Giovannini[a]

[a] *Department of Civil, Environmental and Mechanical Engineering, University of Trento*

[b] *Royal Netherlands Meteorological Institute (KNMI), De Bilt, The Netherlands*

[c] ~~*Department of Earth Sciences Ardito Desio, University of Milan*~~

[d] *Institute of Atmospheric Sciences and Climate, National Research Council of Italy, CNR-ISAC, Bologna*

[e] *Institute of Atmospheric Sciences and Climate, National Research Council of Italy, CNR-ISAC, Padua*

Corresponding author: Lorenzo Giovannini, lorenzo.giovannini@unitn.it

ABSTRACT: Elongated and quasi-stationary deep convective rainbands capable of producing heavy precipitation are often observed over the Italian Alps. Such features occurred in the final and most intense phase of the Vaia storm, on the evening of 29 October 2018. Vaia was an extreme storm, causing floods, landslides and extensive forest damage in several locations of the eastern Italian Alps. In the present work, the thermodynamic conditions favorable for the formation of the rainbands are investigated through semi-idealized numerical simulations performed with the Weather Research and Forecasting (WRF) model. In particular, the influence of wind speed and direction, stability and relative humidity on the development of rainbands is investigated, using different idealized sounding profiles and an idealized smooth ridge. First, a sensitivity analysis with simulations with 1, 0.5, and 0.2 km grid spacing highlights that WRF is able to reproduce the development of deep banded convection over the idealized smooth ridge and that results are independent of the model resolution. Rainbands appear as horizontal roll-like circulations with updrafts reaching altitudes up to 6–7 km MSL and varying their position in time. Then, various sensitivity experiments show that band-shaped convection is favored in the presence of unidirectional low-level wind shear, especially with the alignment of wind shear and wind vectors, and weakly unstable layers above. The presence of convective inhibition in the boundary layer is fundamental for constraining the release of convection over the idealized ridge. Conversely, strong instability or saturated layers in the higher layers disrupt the convective organization.

1. Introduction

Banded orographic convection is frequently observed over different mountainous regions, usually assuming the shape of quasi-stationary rainbands capable of producing highly localized and persistent precipitation, locally increasing the hydrogeological risk. Rainbands can originate both in the windward slope of a ridge (upwind bands) or downstream of topographic disturbances (downwind bands). Upwind orographic rainbands were for example observed in western Kyushu, Japan (Yoshizaki et al. 2000), over the Cevénnes region in France (Miniscloux et al. 2001; Cosma et al. 2002; Anquetin et al. 2003), the Coastal Range in western Oregon (Kirshbaum and Durran 2005a), the Appalachians in the USA (Miller 2012), and in the United Kingdom (Barrett et al. 2016).

The features of orographic rainbands are determined by both the characteristics of the underlying terrain and the thermodynamic conditions of the impinging flow. The thermodynamic conditions of the impinging flow control the propensity of convection to organize in rainbands, whereas orographic features affect their location and persistence. In this regard, Yoshizaki et al. (2000) showed that the deep rainbands (updrafts up to 5–6 km) observed in western Kyushu were generated downstream of small orographic obstacles and were favored by mesoscale convergence. The numerical simulations presented in Cosma et al. (2002) and Anquetin et al. (2003) showed that the rainbands observed over the Cevénnes region in Miniscloux et al. (2001), embedded into a larger-scale stratiform rain pattern, were initiated by the contemporary effect of mountain waves and lee-side convergence induced by tall and narrow terrain disturbances. The effects of small-scale topographic features on rainbands were extensively investigated through idealized numerical simulations in Kirshbaum et al. (2007b) and Fuhrer and Schär (2007), highlighting that the generation of lee waves by small-scale orography is fundamental for anchoring bands in a fixed position, concentrating heavy rainfall over specific locations. On the other hand, Schumacher et al. (2015), analyzing the results of simulations with different degrees of terrain smoothing for a snowband case study in the lee of the Rocky Mountains, hypothesized that the main mechanism for their development was not related to small-scale orography, but to the ascent over a larger-scale terrain slope. Consistent results, with limited sensitivity of precipitation to smoothing the orography, are reported in Schneider et al. (2018), who investigated the impact of terrain on precipitation in different case studies over the Black Forest (Germany) and the Vosges (France). These results imply a limited predictability of these bands (i.e., the successful simulation of their main characteristics, including their persistence, strength and location). On the other hand, the rainband predictability is favored when their development is connected to strong terrain forcing, provided that the model spatial resolution is fine enough for reproducing the relevant topographic details (Cosma et al. 2002; Barrett et al. 2015).

The skills of NWP models in reproducing orographic banded convection are affected not only by the terrain characteristics and their representation in the model but also by the ability of the simulation to reliably capture the characteristics of the flow impinging on the mountain range. In this regard, Cosma et al. (2002), in their simulations of a rainband episode in the Cévennes area, noted that the structure and intensity of the rainbands were dependent on the upwind meteorological conditions. Barrett et al. (2015, 2016), simulating different orographic rainband episodes in the United Kingdom, showed that the predictive skill of convection-permitting forecasts can be highly variable and strongly correlated with the ability of the model to represent the upstream large-scale environment. In particular, Barrett et al. (2015) highlighted that an ensemble approach is required to successfully predict these events, because the rainfall variability is largely modulated by small variations of the large-scale flow.

Given the strong sensitivity to the thermodynamic conditions of the impinging flow, it appears of crucial importance to investigate the atmospheric factors ~~mainly~~ influencing the development of banded orographic convection, not only to advance our understanding of these phenomena, but also to improve their prediction. In this regard, the literature mainly focused on shallow orographic banded convection, whereas the evaluation of the atmospheric factors affecting deep banded convection has received less attention. The atmospheric factors affecting shallow orographic banded convection were investigated by means of idealized numerical simulations in Kirshbaum and Durran (2005a,b), showing that the rainbands appeared as shear-parallel convective roll circulations, developing even over smooth terrain. The results highlighted that over smooth terrain bands are more affected by variations in the atmospheric conditions of the impinging flow and develop only in the presence of strong low-level wind shear and weak instability. On the contrary, lee waves generated by small-scale topographic perturbations promote more stationary and intense bands and also develop in the absence of wind shear. Consistent findings were presented by Fuhrer and Schär (2007), who reported the results of a series of idealized simulations of moist flow past a mountain ridge. In particular, ~~Fuhrer and Schär (2007)~~ highlighted that non-stationary banded convection can develop over a smooth ridge if the time scale of the perturbation growth is compatible with the advective time scale. Godart et al. (2009) summarized the atmospheric conditions favorable for the development of shallow orographic banded convection over the Cévennes region from the analysis of data from 79 soundings: low-level potential instability with a more stable layer above around 700 hPa, high relative humidity decreasing with height and a strong low-level wind speed with low directional vertical wind shear were found as favorable ingredients for shallow banded convection.

Banded orographic convection often develops over the eastern Italian Alps, where deep rainbands are observed in the presence of strong and moist southerly currents, usually associated with fall storms caused by an eastward-moving trough in the Mediterranean. An example are the rainbands that developed during the last phase of the extreme ~~Vaia~~ storm on 29 October 2018~~, which~~ caused floods and heavily impacted the river network over the eastern Italian Alps, with 72-h accumulated precipitation exceeding 200-year return period values in many stations in this area (Davolio et al. 2020; Giovannini et al. 2021). The mechanisms of intense orographic precipitation over the southern Alpine slopes have been extensively investigated in the literature, for example in studies related to the Mesoscale Alpine Programme (MAP, Bougeault et al. 2001)~~,~~ nicely summarized in Rotunno and Houze (2007), shedding light on how the complex interaction between the Alpine orography and the impinging flow can modulate the intensity and distribution of precipitation. In this regard, Medina and Houze (2003), analyzing two intense MAP storms, proposed conceptual models for orographic precipitation in stable blocked flow and unstable unblocked flow~~s~~, focusing on the Lago Maggiore area (central Italian Alps). In stable blocked flow, the lowest atmospheric layer does not experience orographic lifting and, if the rising layer of air is stable, precipitation ~~is stratiform~~. On the other hand, in unstable unblocked flow, orographic lifting also affects the low-level flow, favoring the development of convective cells over the first peaks. More recently, the Hydrological cycle in the Mediterranean eXperiment (HyMeX, Ducrocq et al. 2014) focused on heavy precipitation events in different Mediterranean target areas, including the region affected by the Vaia storm, northeastern Italy~~, where~~ heavy ~~precipitation episodes are~~ typically associated with intense low-level southeasterly flow (usually named sirocco in this geographical area) from the Adriatic Sea (Ferretti et al. 2014; Miglietta and Davolio 2022). Coherently with Medina and Houze

(2003), Davolio et al. (2016) highlighted that, in these conditions, an easterly barrier flow develops ahead of the Alps, as a consequence of the low-level flow-blocking of the incoming southeasterly wind. The dynamical characteristics of the impinging southerly flow strongly influence the location of precipitation~~, distinguishing between situations of~~ persistent blocked flow, ~~in which~~ rainfall is concentrated over the plain due to the low-level convergence between the barrier wind and the impinging southeasterly flow upstream of the orography~~, and situations in which~~ the sirocco wind progressively penetrates inland, removing the barrier wind and establishing flow-over conditions, ~~with~~ heavy precipitation over the Alps. In the former case, ~~when~~ the southeasterly wind is conditionally unstable, deep convection may develop over the plain (Manzato et al. 2015; Miglietta et al. 2016; Ricchi et al. 2021). The latter case, ~~in~~ which the Vaia storm ~~can be categorized~~, is ~~favored with~~ strong southeasterly winds and a nearly moist neutral profile in the low levels. Convection is inhibited over the plain, but can develop over the Alps due to orographic lifting (Davolio et al. 2016; Stocchi and Davolio 2017).

Despite a considerable number of ~~works~~ focusing on orographic precipitation over the Italian Alps, the literature still misses investigations of the dynamic mechanisms of banded orographic convection ~~in this region~~. In this region, recent works concentrated on the hydrological impacts of intense banded convection episodes (Borga et al. 2007) or on the generation of cloud bands downwind (north) of the Alpine ridge (Siedersleben and Gohm 2016; Kirshbaum and Schultz 2018).

In this paper, the atmospheric conditions favorable for the formation of intense rainbands over the Italian Alps are analyzed using idealized simulations, following the approach proposed by Kirshbaum and Durran (2005a,b) and Fuhrer and Schär (2007). In contrast with previous works, here we analyze an intense Alpine event characterized by deep convection, instead of focusing on shallower convective episodes. In addition, the sensitivity to the model numerical resolution is discussed. In fact, it is still not clear what is the minimum grid resolution needed to correctly simulate these events. Fuhrer and Schär (2007) suggest that rainband features are dependent on grid spacing if the topographic details that can initiate convection are not captured by the model, as in the case of smooth topography with thermal perturbations in the upstream flow.

The article is structured as follows: Section 2 provides a description of the case study used as starting point for our analysis. Section 3 illustrates the thermodynamics features of the flow impinging on the Alps. Section 4 presents the idealized simulation setup used for the different sensitivity tests. Simulation results are reported in Section 5, and conclusions are drawn in Section 6.

2. Banded convection during the Vaia storm

Banded convection is a striking feature during fall storms over the southern flanks of the Alpine ridge. An intense banded convective event occurred on the evening of 29 October 2018 in the presence of strong southeasterly winds, during the so-called Vaia storm, an extreme event that caused floods, landslides and forest damages over the eastern Italian Alps (Cavaleri et al. 2019; Davolio et al. 2020; Giovannini et al. 2021).

These rainbands, which can be appreciated from the radar reflectivity referring to 1930 UTC ~~reported in~~ Fig. 1, were accompanied by strong rainfall intensity (up to 60 mm h^{-1}) for about two hours. Their intensity distinguishes this case from previous literature studies (e.g., Kirshbaum and Durran 2005a; Fuhrer and Schär 2007), usually characterized by moderate precipitation rates. Although the present study takes as starting point the atmospheric conditions of this particular event, which represented one extreme case with intense convection, the results can be generalized to other banded episodes that occurred over the southern flanks of the Alps, which are often characterized by similar atmospheric conditions.

This heavy precipitation episode was caused by the deepening of a mid-tropospheric trough over western Europe extending from Scandinavia across France and the Iberian Peninsula, causing the development of a surface low pressure close to the Algerian coasts on 28 October, which then moved northward and reached northwestern Italy (Davolio et al. 2020), where the surface pressure minimum deepened to 977 hPa. This synoptic situation favored the development of intense and moist southeasterly wind over the Adriatic Sea (sirocco). Heavy precipitation and strong wind gusts characterized this phase of the storm, with consequent damage in the eastern Italian Alps. The orographic rainbands analyzed in this study developed in this phase, on the evening of 29 October, associated with the passage of the cold front over the eastern Alps. Further details on this meteorological event and its meteorological simulation can be found in Davolio et al. (2020) and Giovannini et al. (2021).

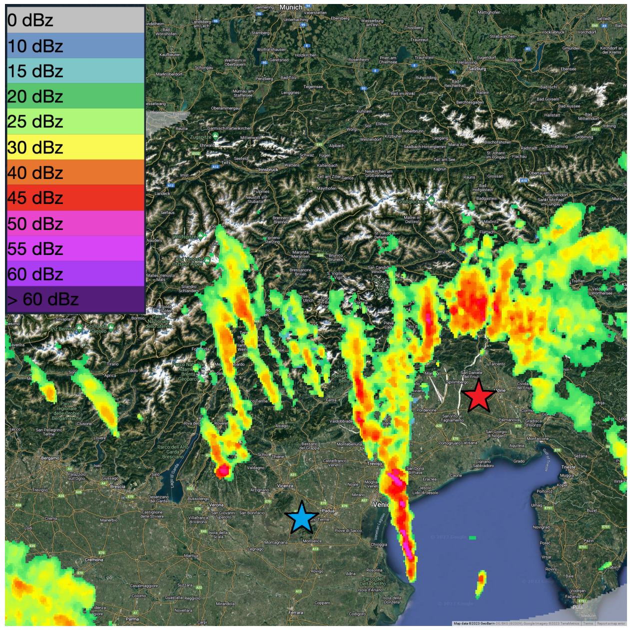

FIG. 1. Vertical maximum intensity (dBZ) over the eastern Italian Alps from the Teolo radar (Environmental Protection Agency of the Veneto region) referring to 1930 UTC 29 October 2018. The red star represents the position of the radiosounding in Udine-Rivolto, and the blue star represents the position of the Teolo radar. Image provided by the Italian Civil Protection Department.

3. Upstream flow

The semi-idealized numerical simulations, aimed at analyzing the rainband sensitivity to atmospheric parameters, are initialized by assigning an upstream input sounding as inflow boundary condition containing the main characteristics of the impinging flow. Considering that this analysis is inspired by the observation of orographic rainbands during the Vaia storm on 29 October 2018 over the eastern Italian Alps, the most representative sounding of this event is that recorded at Udine-Rivolto (red star in Fig. 1). In particular, the 1800 UTC sounding has been chosen as reference for all the following analyses, because the most organized bands on radar images occurred between 1900 and 2000 UTC (Fig. 2). The skew T–log$p$ diagram in Fig. 2 shows a shallow stable layer near the ground, topped by a well-mixed layer between the Lifting Condensation Level (LCL) and the Level of Free Convection (LFC), evaluated for a surface parcel. A potentially unstable layer is located between the LFC and a strong inversion, which is visible at about 520 hPa and affects the vertical development of convection. This 3-km deep layer represents the unstable environment that favored the development of convective motions. The degree of potential instability is even clearer looking at the vertical profile of equivalent potential temperature (Fig. 2b), which shows a region with $\partial\theta_e/\partial z < 0$ between 1.5 km and 4.5 km MSL. The wind speed vertical profile (Fig. 2b) is characterized by a region of strong wind shear in the lowest 3 km, highlighting the presence of a low-level jet, due to the strong southeasterly wind preceding the passage of the cold front (Giovannini et al. 2021). As for the thermodynamic parameters describing the stability of the atmosphere, the surface-based CAPE has a value of 704 J kg^{-1} and the convective inhibition (CIN) of 43 J kg^{-1}. The presence of CIN highlights the importance of the mountain ridge for convection initiation. The vertical relative humidity profile (Fig. 2b) shows two near-saturated layers, located between 1 and 1.5 km MSL and between 3 and 4 km MSL.

a. Simplification of the upstream sounding and control sounding

To suitably design the different sensitivity experiments, a slight simplification of the upstream sounding is required. Different studies have investigated the characteristics of orographic rainbands using highly simplified soundings (e.g. Kirshbaum and Durran 2005a; Kirshbaum et al. 2007b; Fuhrer and Schär 2007). These soundings were often characterized by a two-layer atmospheric structure, with a constant relative humidity profile: a lower layer with $\partial\theta_e/\partial z < 0$ and an overlying absolute stable layer. Conversely, in this study, the upstream conditions used for the simulations closely represent the real flow, thus representative of the atmospheric conditions typical of intense banded convective events under sirocco winds, as in the case of the Vaia storm. In particular, the control simulation is based on a slightly simplified version of the original Udine-Rivolto sounding. The control sounding (CTRL) contains a southerly flow and a three-layer stability structure in the lowest 5.2 km of atmosphere, as shown in Fig. 2b. Thus, in the control sounding the rotation of wind with height (Fig. 2a) is neglected. The lowest 1.2 km of the atmosphere are characterized by a dry Brunt-Väisäla frequency $N_1^2 = 0.00008$ s^{-2}; a more statically stable layer with $N_2^2 = 0.00019$ s^{-2} is located between 1.2 and 2 km MSL, topped by a third layer with $N_3^2 = N_1^2$ up to 5.2 km MSL. Above the strong inversion at 5.2 km MSL, the values of potential temperature have been kept almost unvaried with respect to the original sounding, with only a slight smoothing. Similarly, the vertical relative humidity and wind speed profiles are a slightly smoother version of the original sounding.

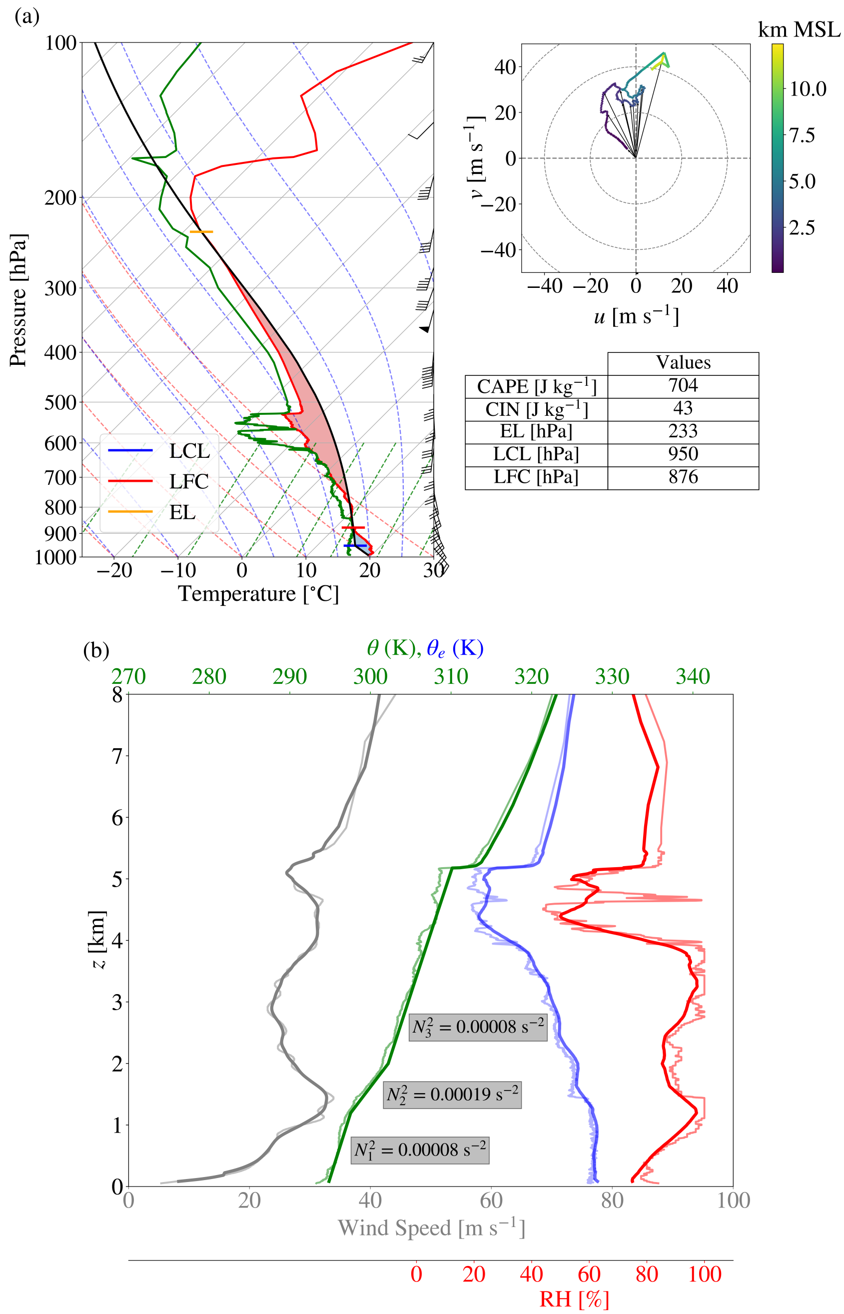

FIG. 2. (a) Skew T–log$p$ diagram of the radio-sounding taken at Udine-Rivolto at 1800 UTC 29 October 2018. Half wind barbs represent 5 m s^{-1}, full wind barbs 10 m s^{-1}, and pennants 50 m s^{-1}. The upper right plot shows the corresponding hodograph, and the table describes the main sounding diagnostics. (b) Vertical profiles of potential temperature θ (green), equivalent potential temperature θ_e (blue), relative humidity RH (red) and wind speed (gray) from the surface up to 8 km MSL. Thin lines show the original Udine-Rivolto vertical profiles, thicker lines the CTRL sounding profiles.

4. Modeling setup

A series of semi-idealized numerical simulations with the Weather Research and Forecasting model (WRF, version 4.1.2, Skamarock et al. 2019) have been performed. Simulations have been carried out using nested domains: the one-way nesting approach has been used for the simulations aimed at investigating the possible dependence of rainband development on grid spacing, in order to obtain independent simulations, whereas the two-way nesting approach has been used for the other simulations. The domain configuration for all the idealized simulations is shown in Fig. 3. An idealized ridge is located at the center of the domains, whose shape has been defined following Kirshbaum and Durran (2005a). The ridge is oriented in the west–east direction, and it is defined by the following expressions:

$$h(x,y) = \begin{cases} \frac{h_0}{16}\left[1+\cos(\pi r)\right]^4, & r \le 1 \\ 0, & \text{otherwise} \end{cases} \tag{1}$$

where

$$r^2 = \begin{cases} \left(\frac{y-y_0}{4a}\right)^2 + \left(\frac{|x-x_0|-B}{4b}\right)^2, & |x-x_0| > B \\ \left(\frac{y-y0}{4a}\right)^2, & \text{otherwise} \end{cases} \tag{2}$$

In Equations (1) and (2) x_0 and y_0 have been set as the center cell of the larger domain, so that $x_0 = y_0 = 600$ km. The other parameters are $a = 18$ km, $b = 12$ km, $B = 45$ km and $h_0 = 1.5$ km. The choice of the maximum altitude h_0 is representative of the pre-Alpine region in the southeastern Alps, and the values of the other parameters allow the definition of a ridge large enough to simulate the bands, but small enough to avoid an unnecessary increase in computational time.

The outermost domain has horizontal dimensions of 1200 km x 1200 km, a horizontal grid spacing of 3 km, and an integration time step of 9 s. The large spatial extent of the outermost domain compared to the size of the ridge was decided to ensure mass conservation and minimize the influence of lateral boundary effects on the precipitation pattern, as highlighted in preliminary simulations with a smaller outer domain. The horizontal grid spacing is 1 km for the second domain, whereas two different spacings, 500 and 200 m, were tested for the innermost domain.

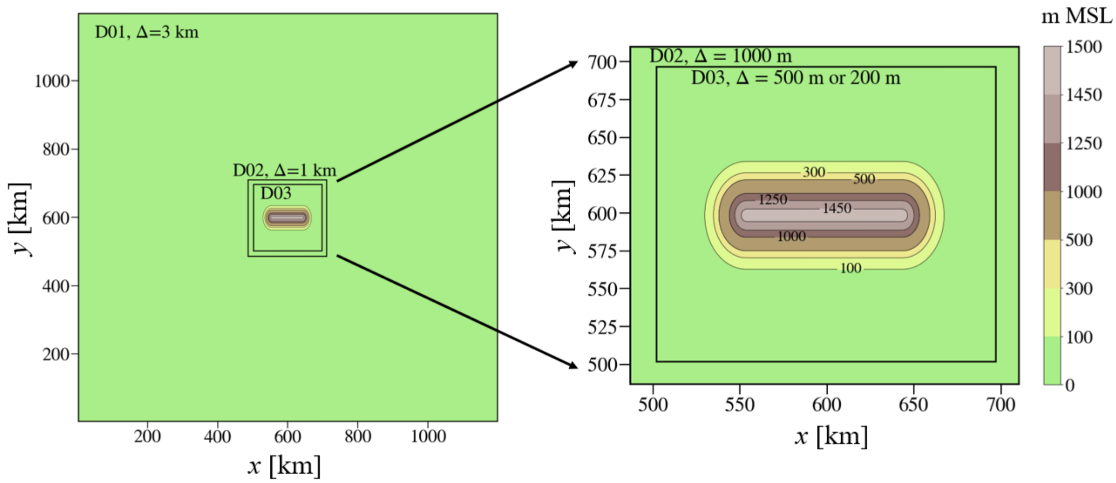

FIG. 3. Model grid configuration and terrain height used for the idealized simulations.

The domain size for the inner domains is 225 km x 225 km for domain 2 and 195 km x 195 km for both the innermost domains. Finally, 66 stretched vertical levels have been used, with higher resolution close to the ground: 17 vertical levels are located in the first 500 m over the terrain height. Simulations start at 1800 UTC 29 October 2018 and run for 12 hours.

The set of parameterizations used for the simulations are the WSM6 scheme (Hong and Lim 2006) for the microphysics, the Yonsei State University planetary boundary layer scheme (Hong et al. 2006), the revised Monin–Obukhov scheme (Jiménez et al. 2012) for the surface layer and the Noah-MP land-surface model (Yang et al. 2011). The Rapid Radiative Transfer Model (Mlawer et al. 1997) is used for the long-wave radiation and the Dudhia (1989) for the short-wave radiation. The convection parameterization is turned off, because the model is able to explicitly resolve it at the resolution adopted. Open lateral boundary conditions have been set in the south–north direction and periodic in the west–east direction. Regarding the options for model dynamics, the top boundary is a rigid horizontal lid located at an altitude of 25 km, associated with a 5-km deep Rayleigh-damping layer used to prevent the reflection of gravity waves created by the orography.

Previous works focusing on idealized simulations of upwind orographic rainbands typically neglected the Coriolis effect (e.g., Kirshbaum and Durran 2005a,b; Kirshbaum et al. 2007b; Fuhrer and Schär 2007). On the other hand, differences between simulations with and without the Coriolis effect were highlighted in modeling studies of orographic blocked flow, considering in particular a deflection to the left of the upstream flow (e.g., Schneidereit and Schär 2000; Chen and Lin 2004;

Name	Dry stability	Wind Speed	Wind Direction	Relative Humidity
R200	Original	Original	S	Original
R500	Original	Original	S	Original
CTRL	CTRL	CTRL	S	CTRL
V10	CTRL	10 m/s	S	CTRL
V20	CTRL	20 m/s	S	CTRL
V30	CTRL	30 m/s	S	CTRL
V10_SHEAR	CTRL	Idealized, 10 to 40 m/s in 5 km	S	CTRL
210°	CTRL	CTRL	210° N	CTRL
UDINE_ROT20	CTRL	Original	Original , rot. 20° cw	CTRL
SHEAR_TILTED	CTRL	Idealized, weaker low-level shear	SW vertical shear	CTRL
N1_000001	$N_1^2 = 0.00001\ \mathrm{s}^{-2}$	CTRL	S	CTRL
N1_00004	$N_1^2 = 0.00004\ \mathrm{s}^{-2}$	CTRL	S	CTRL
N1_00015	$N_1^2 = 0.00015\ \mathrm{s}^{-2}$	CTRL	S	CTRL
N1_00004_N3_00004	$N_1^2 = N_3^2 = 0.00004\ \mathrm{s}^{-2}$	CTRL	S	CTRL
N1_00004_N3_00009	$N_1^2 = 0.00004, N_3^2 = 0.00009\ \mathrm{s}^{-2}$	CTRL	S	CTRL
N1_00004_N3_00012	$N_1^2 = 0.00004, N_3^2 = 0.00012\ \mathrm{s}^{-2}$	CTRL	S	CTRL
RH_REDUCED5	CTRL	CTRL	S	-5%
RH_INCREASED5	CTRL	CTRL	S	+5%
RH_INCREASED5_LL	CTRL	CTRL	S	+5% below 2.3 km
RH_INCREASED5_UL	CTRL	CTRL	S	+5% above 2.6 km

TABLE 1. List of the simulations analyzed in the present work. The horizontal grid spacing of the inner domain is 1 km for all the simulations, apart from R200 e R500, with a horizontal grid spacing of 200 m and 500 m respectively. cw = clockwise.

Galewsky 2008; Kirshbaum and Schultz 2018). In this regard, Peng et al. (1995) pointed out that the role of the Coriolis effect depends not only on the Rossby number $Ro = U/fL$, where U is a representative velocity of the cross-barrier flow, f the Coriolis parameter and L the half-width of the mountain range, but also on the Froude number $Fr = U/Nh$, where N is a representative value of the subcrest dry Brunt-Väisäla frequency and h the mountain height. The Froude number, or its inverse, the non-dimensional mountain height $\epsilon = Nh/U$ (Smith 1988), can be used to broadly distinguish between flow-blocked ($Fr < 1$) and flow-over ($Fr > 1$) regimes. Peng et al. (1995) showed that, with a large Rossby number, the effect of the Coriolis force is small when $Fr > 1$, whereas when $Fr < 1$ Coriolis cannot be neglected. The control sounding used in this study is characterized by $Fr \simeq 1.9$, whereas $Ro \simeq 6$, using $U = 25$ m s^{-1}. Moreover, in all the simulations presented in this work $Fr > 1$, with the only exception of V10, where a constant wind speed of 10 m s^{-1} is used and $Fr \simeq 0.75$. Based on these considerations, the Coriolis effect has not been considered in this study.

A background thermal noise embedded in the low-level flow is used to release the instability characterizing the upstream flow, perturbing the initial state potential temperature field of the outermost domain with random perturbations in a range of ±0.1 K in the lower 4 vertical levels.

The decision to apply perturbations only in the outer domain was guided by the goal of investigating the sensitivity to horizontal resolution, which requires for consistency that an equal perturbation field characterizes all the three simulation domains.

a. *Setup of the sensitivity experiments*

The sensitivity tests to evaluate the influence of model resolution were conducted using the original Udine-Rivolto sounding (thinner lines in Fig. 2b). The only simplification regards the removal of directional wind shear, whose effect has been explored subsequently. Therefore, a southerly wind with the same wind speed profile as the reference sounding has been defined.

Apart from this exception, all the other simulations have been performed with the CTRL sounding (Fig. 2) or modifications applied to the latter. Table 1 presents a summary of the simulations shown in the next sections, briefly listing their main features. The simulations differ in some of the characteristics of the CTRL sounding: in particular modifications have been applied to wind speed, wind direction, atmospheric stability, and relative humidity vertical profiles. The choice to apply these modifications to the CTRL sounding has been mainly guided by the results of previous literature studies, with the aim of investigating the role of the atmospheric parameters that were found to mostly affect band development.

5. Results and discussion

a. *Sensitivity to horizontal resolution*

The sensitivity of simulated rainbands to model horizontal resolution has been tested by analyzing the results of R500 and R200 (Table 1), in particular comparing the results from domain 2 (1000 m horizontal grid spacing) with those from domain 3 (500 m or 200 m grid spacing).

Figure 4 shows a horizontal section of rain liquid mixing ratio at 2 km MSL for both R200 and R500 and reveals the characteristics of the simulated convective structure. An altitude of 2 km MSL allows the precipitation field to be well captured. The convection patterns ~~shown in~~ Fig. 4a and Fig. 4b are not the same, even if they both refer to a domain with grid spacing of 1000 m, as they come from two different simulations initialized with different random thermal perturbations. Conversely, a comparison between Fig. 4a and Fig. 4c shows that, even without a feedback effect between the nested domains, a similar precipitation field is simulated at 1 km and 500 m grid spacing. The same considerations can be drawn by comparing Fig. 4b and Fig. 4d (1000 m and 200 m grid spacing respectively). The simulations with higher resolution are able to simulate more elongated and better-defined bands, with a higher degree of detail. However, their position is in close agreement with those simulated at 1 km grid spacing, suggesting that, in this case, the position and spacing of the orographic rainbands do not depend on the model resolution.

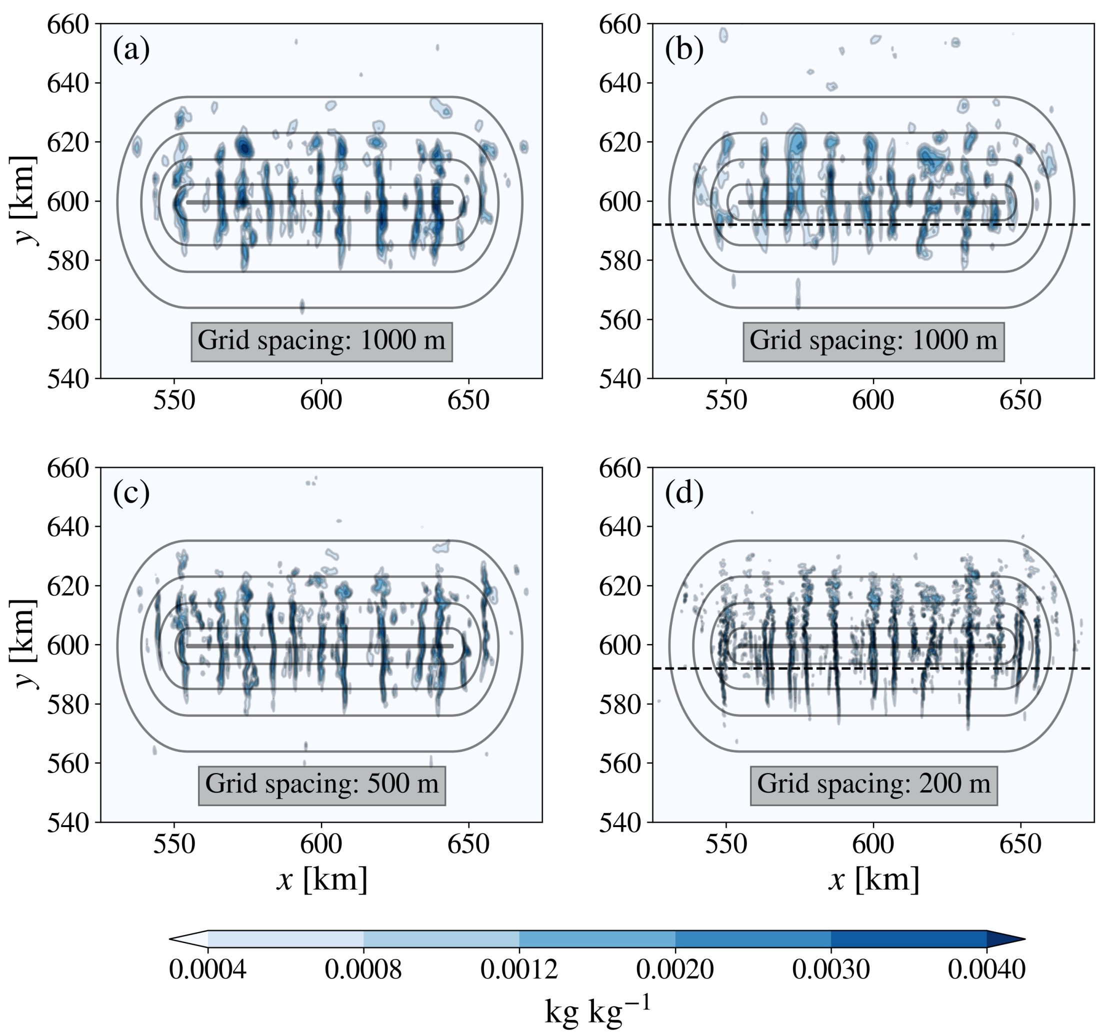

FIG. 4. Rain liquid mixing ratio q_r at 2 km MSL and t = 6 h for (a) domain 2 (grid spacing 1000 m) of R500, (b) domain 2 (grid spacing 1000 m) of R200, (c) domain 3 (grid spacing 500 m) of R500, (d) domain 3 (grid spacing 200 m) of R200. Dashed lines show the sections used for the Fourier analysis of the one-hour accumulated rainfall amounts reported in Fig. 5, corresponding to y = 592 km. Topographic contour intervals are at 100, 500, 1000, 1400 and 1500 m MSL.

The independence of the simulated bands from numerical resolution is also quantitatively evaluated by performing a Fourier analysis of the one-hour accumulated rainfall amounts at t = 6 h along the section at y = 592 shown in Fig. 4 for R200. Figures 5a,b show the one-hour accumulated rainfall amounts along this section in the two inner nested domains (domains 2 and 3 with 1000 m and 200 m grid spacing, respectively) and the corresponding Fourier spectrum. A good agreement between the one-hour accumulated rainfall amounts of the two domains can be seen (Fig. 5b). Therefore, once the same boundary conditions are assigned from the external domain 1, the model simulates the rainbands in the same positions in the two inner domains, regardless of the horizontal resolution adopted. This result is confirmed by the associated Fourier spectra, which show a remarkable agreement in the position of the peaks (Fig. 5a). In particular, the spectrum is characterized by three peaks. The first peak has a frequency of 0.008 km^{-1}, which corresponds to the size of the ridge (125 km) and is related to the orographic precipitation, resulting from the mean uplift of the flow generated by the ridge. The second region of higher spectral energy has a frequency between 0.1 and 0.2 km^{-1}, describing the typical spacing between rainbands in the simulation, which ranges from 6 to 8 km. This range is consistent with Kirshbaum et al. (2007a), who found band spacing between 5 and 10 km in their simulations over an idealized ridge containing a spectrum of terrain scales. On the other hand, variable spacings were reported in real case studies, for example larger spacing was observed by Schumacher et al. (2010, 2015) for a snowband episode downwind of the Rocky Mountains. Finally, the third peak corresponds to a wavelength of about 3 km and it is connected to the development of secondary roll circulations. Fourier analyses of the one-hour accumulated rainfall amounts taken along different west–east cross sections provided the same peaks, with variations of their amplitude, suggesting that the previously described peaks are related to the specific characteristics of the rainbands and not to local orographic features.

This initial analysis suggests that an optimal compromise for simulating orographic rainbands is probably a grid spacing of 500 m, but a grid spacing of 1 km is also reasonable and sufficient to capture the main characteristics of the convective rainbands. Therefore, considering the large number of simulations performed in this study, it was decided to adopt a grid spacing of 1 km to test the influence of atmospheric factors on this type of convective mode.

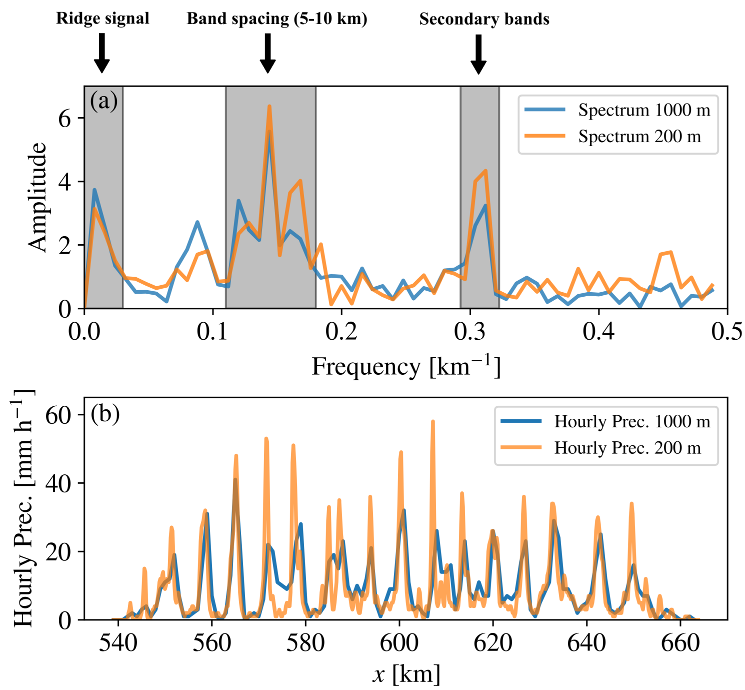

Fig. 5. (a) Fourier spectra of the one-hour accumulated rainfall amounts and (b) one-hour accumulated rainfall amounts at t = 6 h along a section at y = 592 km for domains 2 (1000 m grid spacing) and 3 (200 m grid spacing) of R200.

b. CTRL Simulation

A control simulation (CTRL) has been run using the idealized upstream sounding shown in Fig. 2b. The results of this simulation are used for comparison with other simulations initialized with different idealized soundings. They also provide insights into the three-dimensional structure characterizing such intense orographic rainbands. The rainfall pattern is evaluated at t = 6 h and t = 9 h ~~in Fig. 6~~ both as rain liquid mixing ratio (Figs. 6a,b) and as one-hour accumulated rainfall amounts (Figs. 6c,d). These are representative time steps to analyze the development and evolution of the rainbands. The slightly lower relative humidity compared to the observed sounding decreases the instability of the flow and allows the simulation of more organized rainbands compared to R200 and R500 at t = 6 h (cf. Figs. 4a,b and Fig. 6a). This aspect will be better highlighted by the analysis of the simulations focusing on the sensitivity to relative humidity.

The rain mixing ratio ~~shown in~~ Figs. 6a,b shows that the simulated rainbands can extend up to 40 km in the south–north direction. Moreover, the comparison between q_r patterns at t = 6 h and t = 9 h highlights that rainbands change their location with time and are not stationary. In fact, the initiation mechanism caused by the growth of thermal perturbations depends on their advection and is not stationary, in the presence of a completely smooth ridge, as also highlighted in Kirshbaum and Durran (2005a) and Fuhrer and Schär (2007). Moreover, it can be seen that at t = 9 h convection tends to be less organized, with some bands that seem to merge into larger structures. The non-stationarity of the rainbands is reflected in the one-hour accumulated rainfall

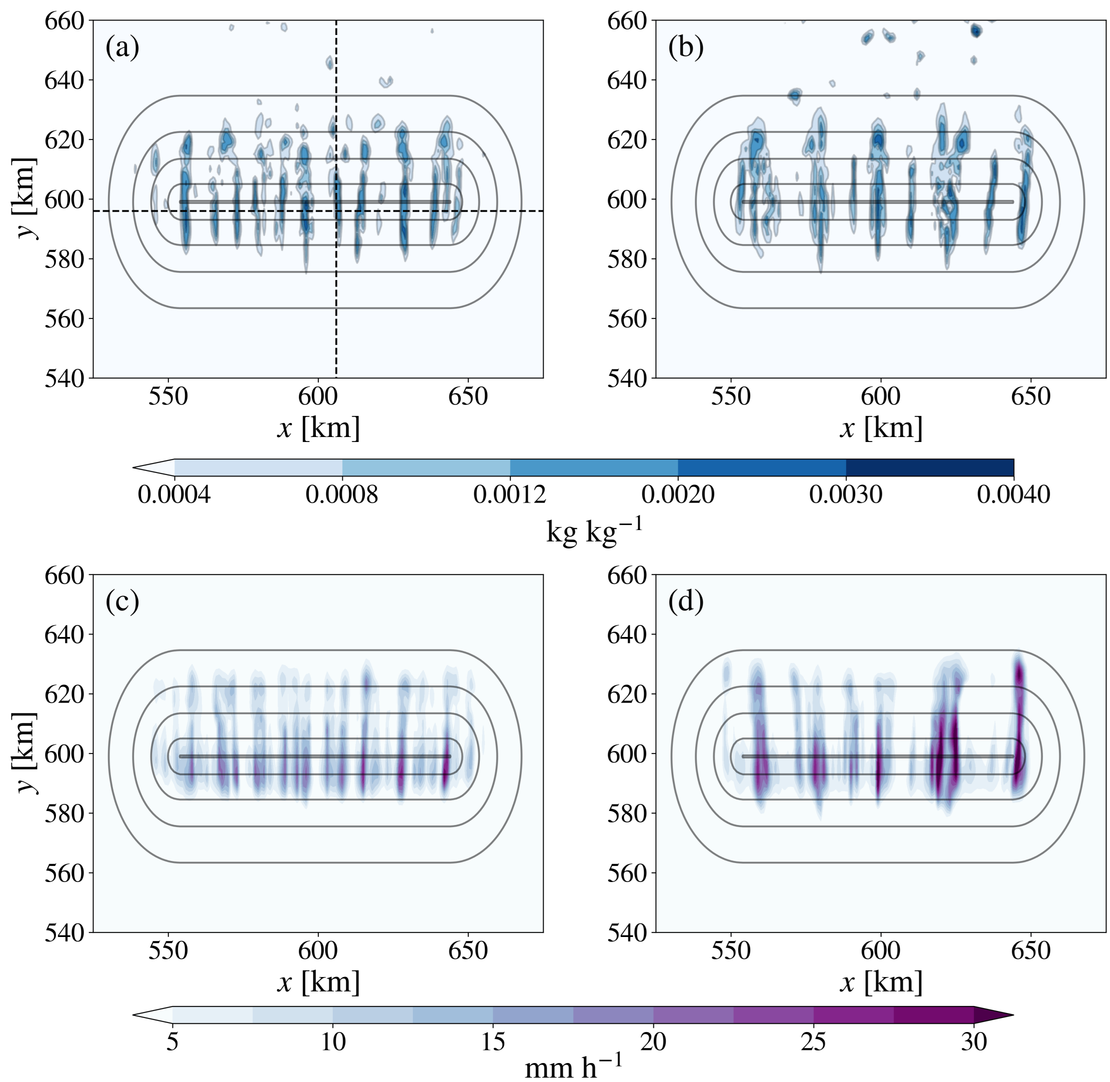

Fig. 6. Rain liquid mixing ratio q_r at 2 km MSL at (a) $t = 6$ h and (b) $t = 9$ h from CTRL; one-hour accumulated rainfall amounts at (c) t = 6 h, and (d) t = 9 h from CTRL. The dashed lines in (a) represent the location of the x–z section shown in Fig. 8a, and of the y–z section shown in Fig. 8b.

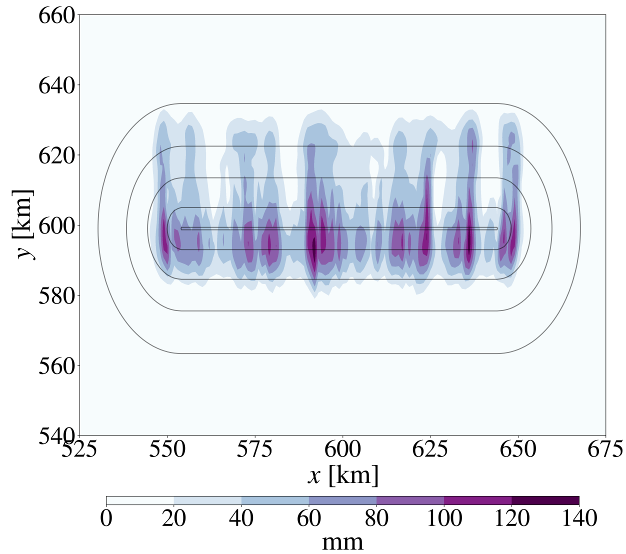

FIG. 7. Accumulated rainfall amounts between t = 6 h and t = 12 h from CTRL.

amounts ~~shown in~~ Figs. 6c,d, where the effect of the rainbands is visible, but it is also clear that the precipitation maxima change their location across the ridge. The effect of the rainbands remains visible also in the total accumulated precipitation between t = 6 h and t = 12 h~~, shown in~~ Fig. 7. Precipitation is distributed over the whole ridge, with peaks, caused by the most intense rainbands, exceeding 100 mm.

To obtain clear insights into the convective band structure, vertical cross-sections in x and y directions over the ridge are analyzed at t = 6 h (Fig. 8). Figure 8a shows the resulting cross section taken in the x–z plane at y = 596 km. The clouds develop in regions of strong updrafts characterized by vertical velocities exceeding 10 m s^{-1} and which extend up to 6–7 km MSL. These updraft regions are surrounded by areas of enhanced subsidence, which leads to cloud dissipation and creates cloud-free and precipitation-free regions. Figure 8b shows a vertical cross-section in the y–z plane along the line shown in Fig. 6a. The updraft develops along the windward side of the ridge, thanks to the saturation of the upward low-level flow, leading to the formation of convective clouds. The clouds are then dissipated by the subsidence induced by the descending flow on the leeward side.

These sections suggest that the rainbands assume a sort of roll-type circulation structure, as also found in other studies in the literature (Kirshbaum and Durran 2005a,b; Fuhrer and Schär 2007). However, the main difference with the bands reported here is in their vertical extent. Most of the previous studies simulated roll vortices as a result of shallow orographic convection, with a vertical extension of 2–3 km, whereas here convection reaches a vertical extension of 6–7 km. Hence, the structure of the roll vortices in the cloud is maintained, but these roll circulations are not confined to the planetary boundary layer and extend further into the middle troposphere. The structure of the bands can be better appreciated ~~in Fig. 8c,~~ showing a three-dimensional view of the rainbands and flow trajectories starting at 1.5 and 5.5 km MSL. High-level trajectories tend to converge towards the subsidence regions, driven by the divergence at the top of the updrafts, increasing their pressure (i.e., decreasing their altitude), whereas low-level trajectories tend to converge towards the rainbands while decreasing their pressure (i.e., increasing their altitude). This structure demonstrates that orographic rainbands are not necessarily related to shallow convection, and the deep convection also explains the higher rain rates simulated in this case, which are well above the values usually simulated in shallow convective cases.

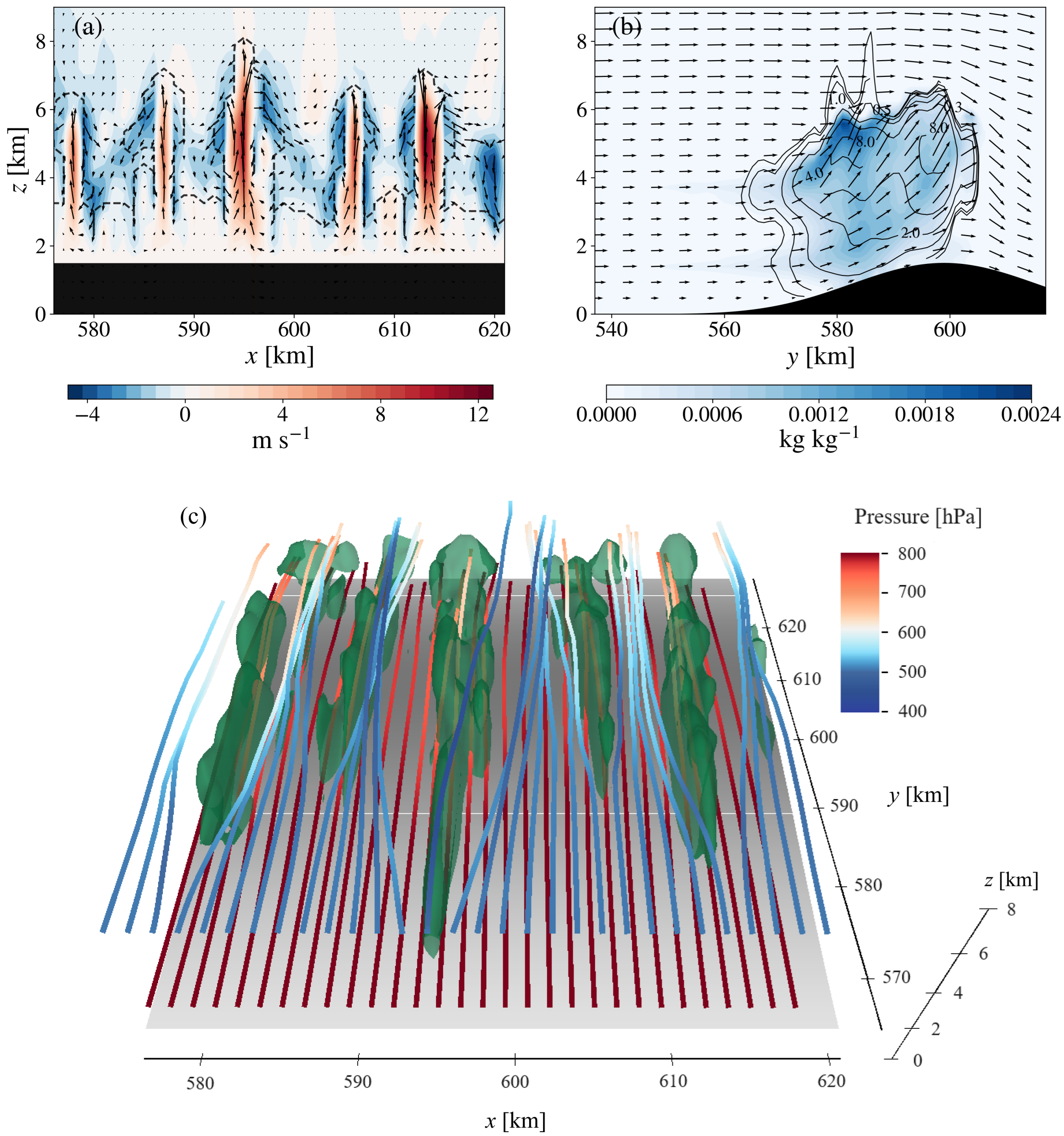

Fig. 8. (a) west–east (x–z) cross-section of cloud liquid mixing ratio q_c (dashed lines), vertical wind speed (colors) and velocity vectors at t = 6 h and y = 596 km from CTRL. q_c contour values are drawn at 10^{-6} and 10^{-4} kg kg^{-1}. Velocity vectors are plotted at each horizontal grid point and every two vertical grid points. The u component has been divided by a factor 2, to better visualize vertical motion. (b) south-north (y–z) cross-section at t = 6 h and x = 606 km of q_c (colors) and w (lines) from CTRL. Velocity vectors are plotted every 2 vertical grid points and 5 horizontal grid points. The v component has been divided by a factor of 8, to get a clearer visualization of vertical motion. (c) Three-dimensional plot of rain liquid mixing ratio q_r (green isosurface at $4{\cdot}10^{-4}$ kg kg^{-1}) and flow trajectories starting at 1.5 m and 5.5 km MSL, colored based on their pressure. The underlying terrain is in gray shading. (c) was obtained with the software Vapor (Li et al. 2019; Visualization & Analysis Systems Technologies 2023).

c. *Influence of upstream atmospheric conditions on band development*

1) Sensitivity to wind speed

The sensitivity of rainbands to wind speed is first analyzed using highly simplified profiles with constant southerly wind speed of 10 m s^{-1} (V10) and 20 m s^{-1} (V20), similarly to Kirshbaum and Durran (2005a). Considering that the first layer of the CTRL sounding has $N \simeq 0.009$ s^{-1} and a depth of 1200 m, the corresponding values of ϵ are 1.35 for V10, favoring the blocking of the low-level flow, and 0.68 for V20, allowing the low-level air to ascend the ridge. The impact of this different behavior on the precipitation pattern is shown in Fig. 9 at t = 6 h and t = 9 h. V10 (Figs. 9a,b) produces highly disorganized and cellular convection present exclusively on the windward side of the ridge, whereas V20 (Figs. 9c,d) shows more elongated rain structures, closer to those shown in CTRL, especially at t = 6 h. The reasons for the differences between the two simulations are highlighted in the cross sections in Figs. 10a,b, referring to t = 6 h, where the θ_e contour lines can be used as an approximation for streamlines. With low wind speed (Fig. 10a), the isentropes in the lower atmosphere intersect the mountain, revealing the flow-blocking regime. An opposite behavior is shown in V20, where the isentropes point out a clear flow-over of the air mass impinging on the mountain (Fig. 10b). The differences between the two simulations are also highlighted by the wind field at 0.1 km AGL ~~shown in~~ Figs. 11a,b, where a large stagnation zone in front of the ridge can be appreciated in V10. The different regimes lead to contrasting cloud developments. In the flow-blocking regime (V10), the condensation in the lower 3 km is a consequence of the interaction between the low-level air, blocked by the ridge, and the impinging flow, which is lifted over the blocked one, causing vertical velocity perturbations that evolve into weak convective motions, once saturation is reached, thanks to the high relative humidity and potential instability above 1 km MSL. The resulting convection is more cellular, and forms about 10 km upstream compared to the convection that develops in CTRL (cf. Figs. 9a,b and Figs. 6a,b). In addition, the weaker wind intensity does not lead to tilted updrafts, causing the weak convection to develop exclusively in the vertical direction. On the other hand, the flow-over situation (V20) favors the formation of more organized convection, similar to the one shown in Fig. 6.

However, in V20 the precipitation pattern does not assume a clear banded structure as in CTRL, but alternates shorter bands with more disordered convective structures. This aspect is partly consistent with Kirshbaum and Durran (2005a), who highlighted that a constant upstream wind

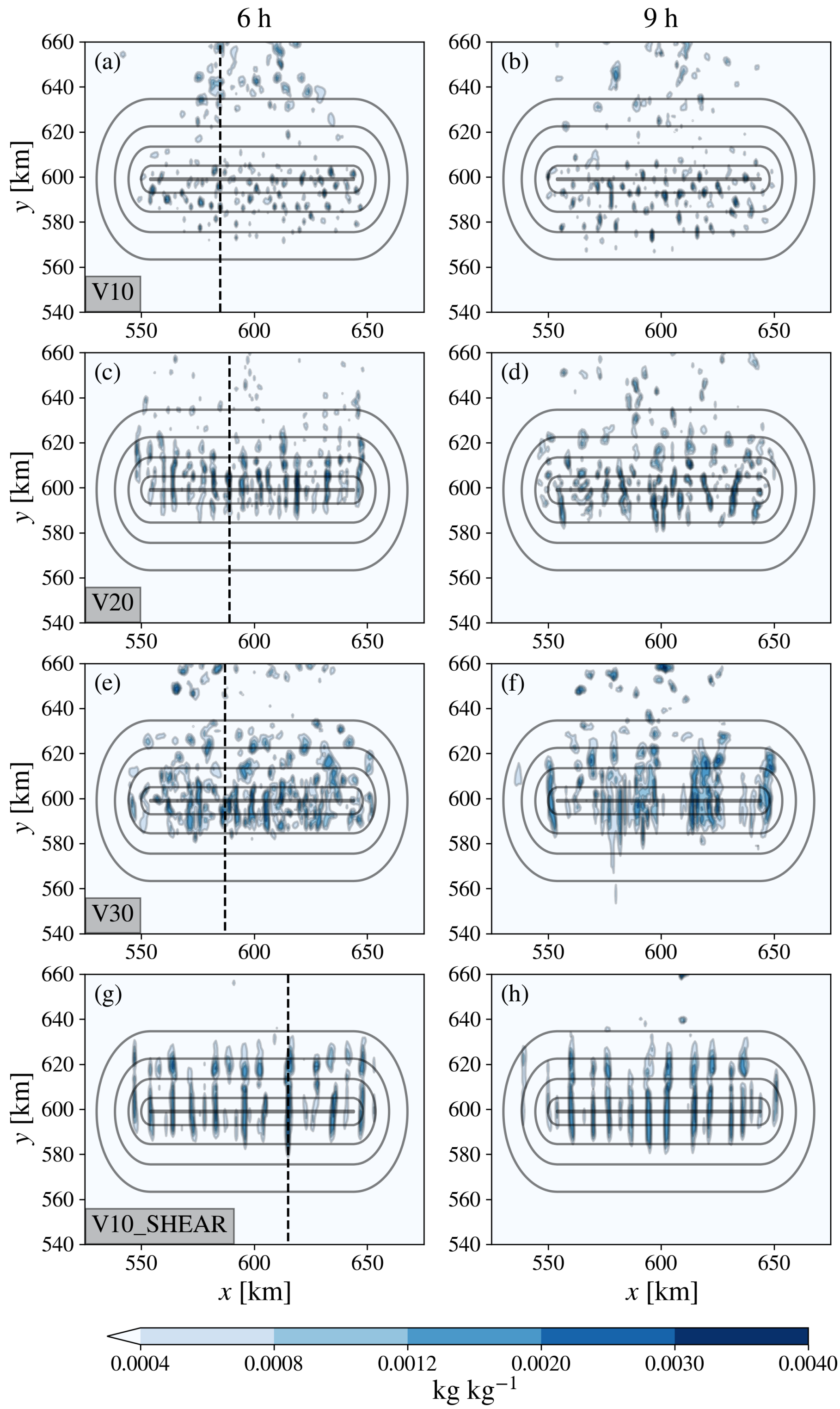

FIG. 9. Rain liquid mixing ratio q_r at 2 km MSL at t = 6 h (left column) and t = 9 h (right column) for (a)–(b) V10, (c)–(d) V20, (e)–(f) V30, (g)–(h) V10_SHEAR. The dashed lines in (a), (c), (e) and (g) represent the location of the y–z sections shown in Fig. 10.

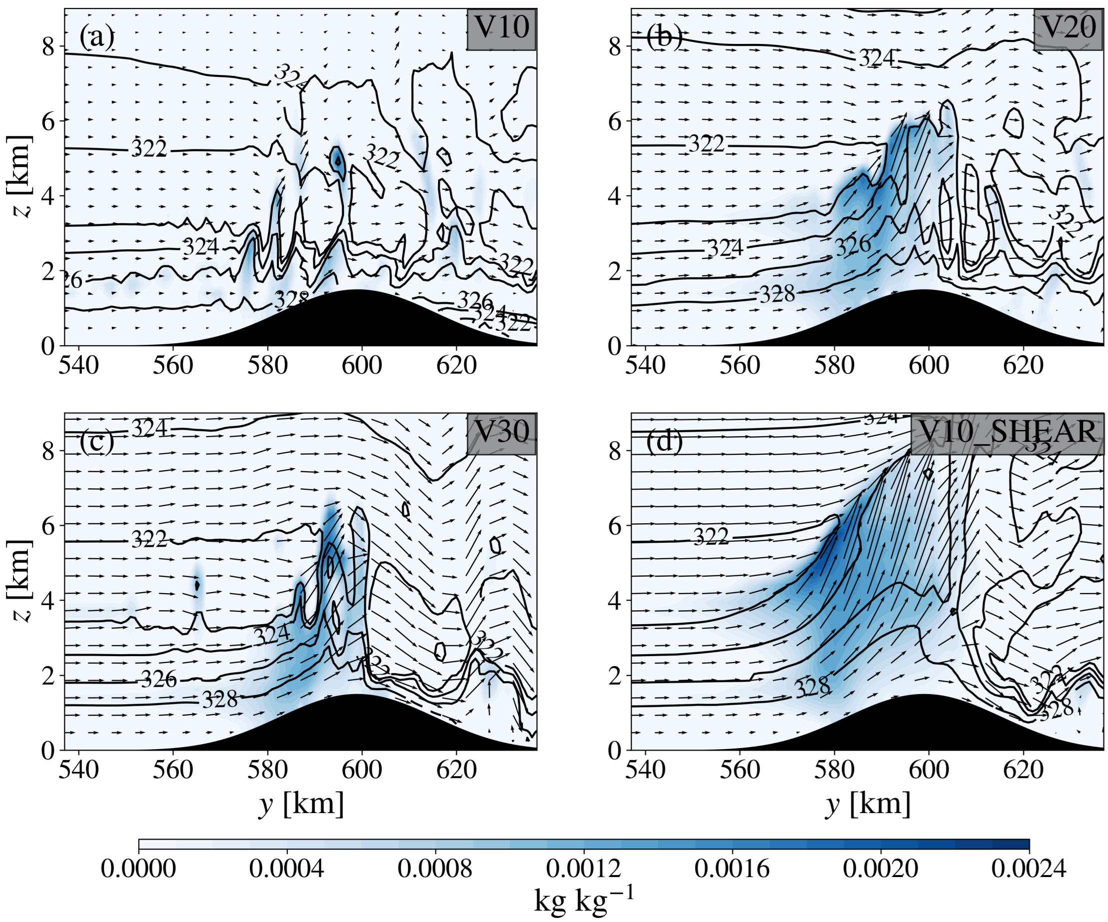

FIG. 10. South–north (y–z) cross sections showing equivalent potential temperature θ_e (contours), cloud liquid mixing ratio q_c (blue shading), and the wind component parallel to the section (arrows) at t = 6 h, for (a) V10 at x = 587, (b) V20 at x = 591, (c) V30 at x = 589 and (d) V10_SHEAR at x = 617. Velocity vectors are plotted every 2 vertical grid points and 5 horizontal grid points. The v component has been divided by a factor of 8, to get a clearer visualization of vertical motion.

velocity profile fails to form organized bands with a pure thermodynamic initiation mechanism and that the presence of low-layer vertical wind shear plays an important role. In this case, banded orographic convection forms even in the simulation with a constant wind speed profile, although with a lower degree of organization than in CTRL, probably favored by the interaction with the ridge, which generates a weak wind shear in the low levels.

To further verify the importance of low-level shear, two other simulations were performed: in the first the constant wind speed is increased to 30 m s^{-1} (V30), whereas the second presents a

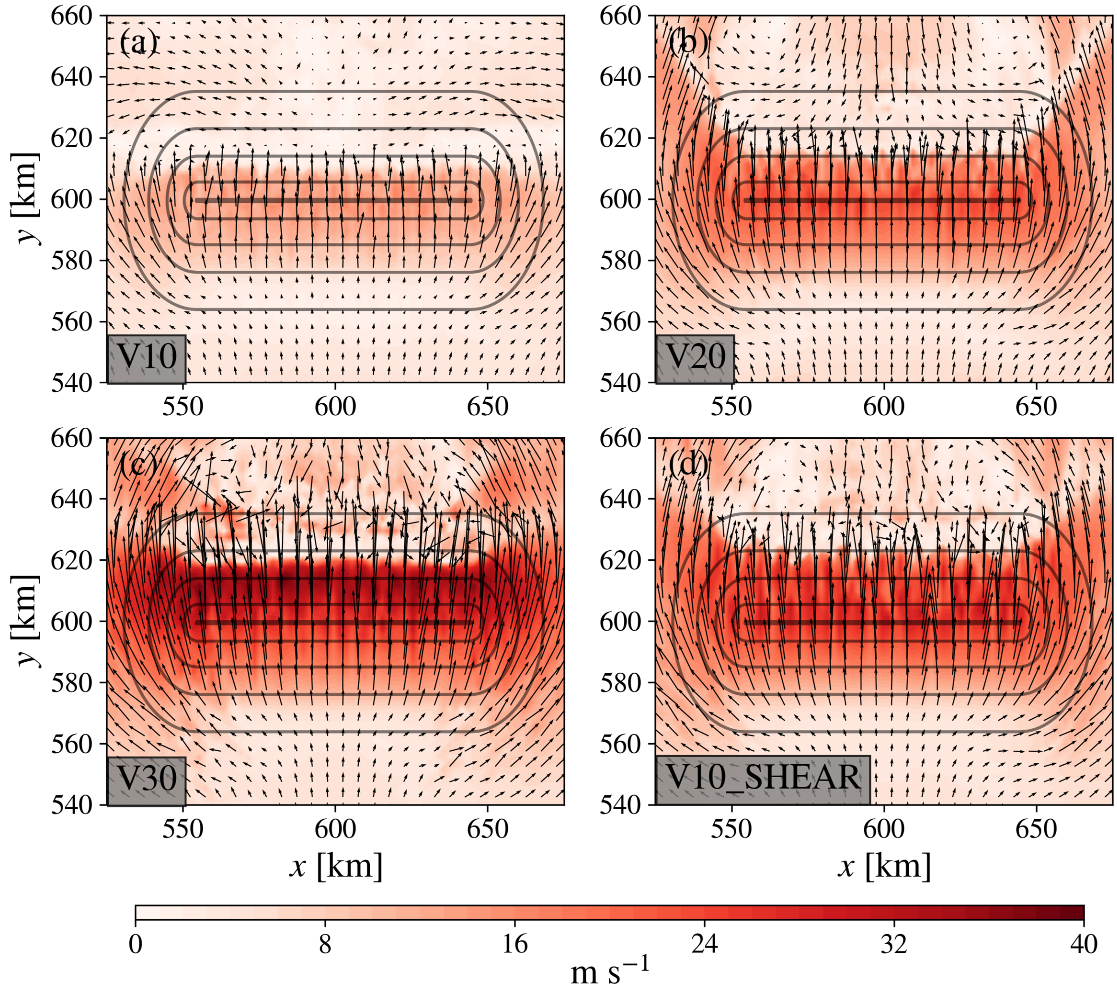

FIG. 11. Horizontal wind field at 0.1 km AGL for (a) V10, (b) V20, (c) V30, and (d) V10_SHEAR.

strong wind shear in the first 5 km to pass from 10 m s^{-1} close to surface to 40 m s^{-1} at 5 km MSL (V10_SHEAR, vertical profile in Fig. 12c).

The results of V30 reveal that an increase in wind speed does not induce a more organized development of the rainbands (Figs. 9e,f). This finding is consistent with Fuhrer and Schär (2007), who highlighted that with strong advection rainbands do not develop, because the advective time scale is not compatible with the time scale of the perturbation growth. The importance of the low-level vertical wind speed shear can be appreciated analyzing the results of V10_SHEAR (Figs. 9g,h), which, instead, develops a clear banded structure, both at t = 6 h and t = 9 h. Its ability to tilt the updrafts ~~is shown in Fig. 10d, highlighting the~~ completely different behavior with respect to V30 (Fig. 10c), even if the wind field at 0.1 km AGL in these two simulations (Figs. 11c,d) share similar features, with slightly higher velocities in V30.

2) Sensitivity to wind direction

Another important aspect to consider is the effect of wind direction and wind rotation with height on the features of the rainbands. In fact, the previous simulations were characterized by a fully southerly flow at all levels (Table 1) and, in the presence of a pure thermodynamic initiation mechanism, it is not obvious that bands can develop in an orderly way when wind direction changes with height.

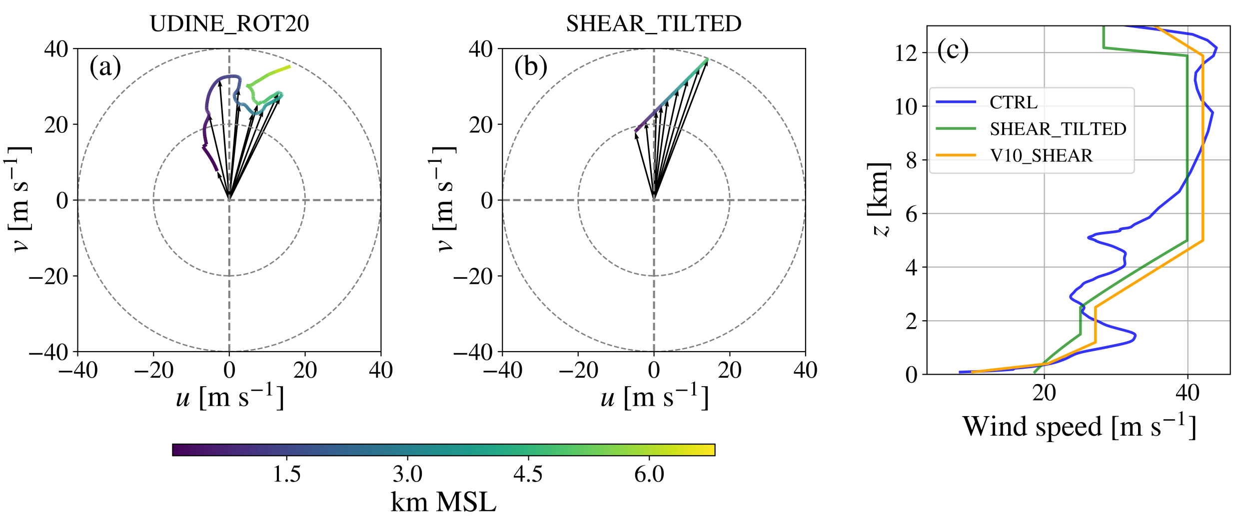

Fig. 12. Hodograph representing wind rotation in the lower 7 km of atmosphere for (a) UDINE_ROT20, (b) SHEAR_TILTED. (c) Wind speed vertical profile for CTRL (blue line), SHEAR_TILTED (green line), and V10_SHEAR (orange line).

This sensitivity analysis is performed analyzing the results of other three simulations. The same wind profile as CTRL (thus with a constant wind direction), but rotated clockwise by 30°, is used in 210°. UDINE_ROT20 has the same wind speed profile as the original sounding shown in Fig. 2a, but its direction has been rotated 20° clockwise along the entire vertical profile. This rotation aimed at simulating an angle of impact with the idealized ridge that is similar to what happened with the eastern Alps during the Vaia storm. The presence of wind rotation with height, as shown by the hodograph in Fig. 12a, is the novelty in this simulation. Finally, SHEAR_TILTED is characterized by an idealized wind speed profile, but comparable to the other two simulations and by unidirectional south-westerly wind shear in the first 5 km of atmosphere (Fig. 12b). The definition of a constant wind shear vector aims at testing whether the preferred alignment of the rainbands follows the mean flow or the wind shear vector. A weaker shear was used in the low-level flow (Fig. 12c), because we wanted to orient the mean wind and wind shear vectors in different directions, otherwise the two vectors would become quickly aligned.

The results of these simulations ~~are shown in Fig. 13 at t = 6 h. Results~~ at t = 9 h are not shown in this case, because some spurious boundary effects were noticed in the simulation output at this time, making the results less reliable. The clearest banded pattern ~~is shown in~~ Fig. 13a, corresponding to 210°, suggest~~ing~~ that a flow characterized by unidirectional wind shear oriented as the mean wind is the most favorable condition. Bands with variable length are present after 6 h, aligned with the impinging southwesterly wind. However, with a tilted impinging flow with respect to the ridge, bands are not so well developed as in the case with perpendicular flow (cf. Fig. 6), especially in the eastern part of the ridge. This behavior is related to the asymmetry of the upstream blocking affecting the low-level flow, as can be seen in ~~Fig. 14, which shows~~ the wind field at 0.1 km AGL and 2 km MSL. Figure 14 highlights that the impinging southwesterly flow experiences stronger low-level blocking in the western sector, increasing the low-level vertical wind shear and thus favoring the development of rainbands in this sector of the ridge.

The interpretation of the results becomes more complicated if a rotation of the wind direction with height is added (UDINE_ROT20). In this case, some bands are simulated in the western sector, whereas convection is more disorganized in the eastern part of the ridge, ~~as shown in~~ Fig. 13b. Therefore, a rotation of the wind with altitude does not favor the convective organization in persistent bands. Moreover, in this simulation the wind shear vector also changes direction with height in the atmospheric layer where saturation occurs, as delineated by the three arrows in Fig. 13b. The wind rotates clockwise in the layer between 2 and 4 km MSL (orange and red arrows), whereas counterclockwise rotation can be detected between 4 and 5.5 km MSL (blue arrow). Thus, the lack of a unidirectional wind shear vector seems to be another aspect that inhibits the organization of roll-type convection over the ridge.

To better evaluate the effect of varying wind direction on band organization, SHEAR_TILTED has been defined with constant directional wind shear and varying wind direction. Also in this case, the simulated rain pattern is less organized, compared to situations with wind shear and wind

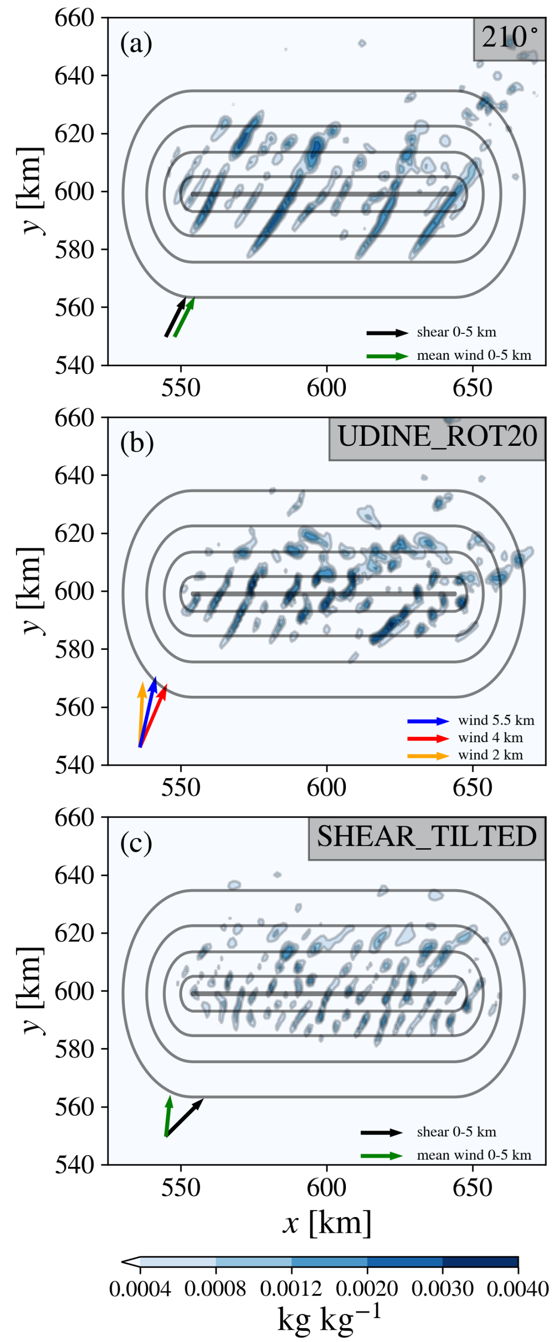

502 FIG. 13. Rain liquid mixing ratio q_r at 2 km MSL at t = 6 h for (a) 210°, (b) UDINE_ROT20, (c) SHEAR_TILTED. In (a) and (c), black arrows indicate the direction of the wind shear vector and green arrows the direction of the mean wind in the layer between the surface and 5 km MSL in 210° and UDINE_ROT20 respectively. In (b), orange, red and blue arrows show the wind vectors respectively at 2, 4 and 5.5 km MSL in UDINE_ROT20.

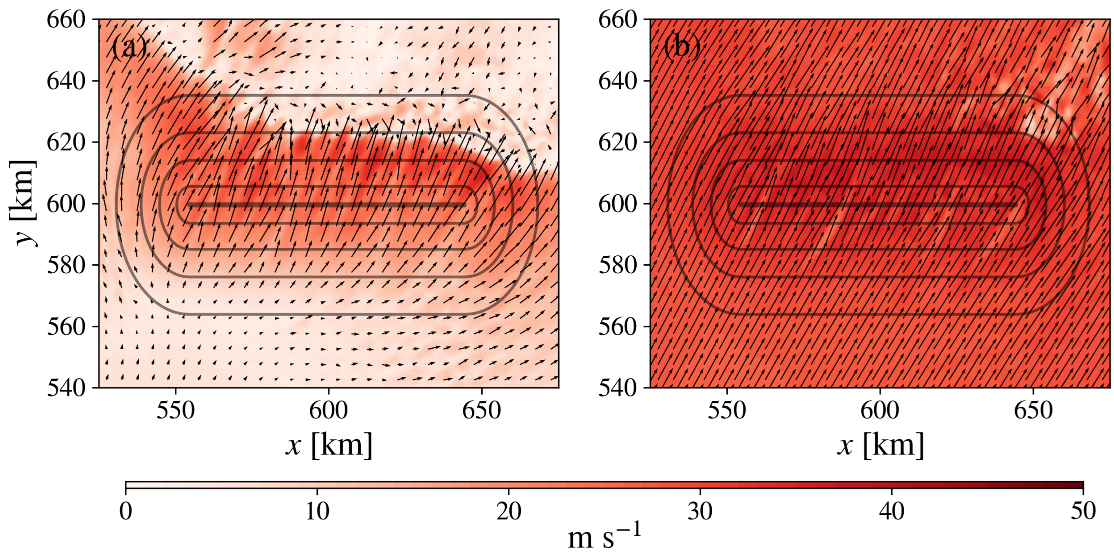

FIG. 14. Horizontal wind field for 210° at (a) 0.1 km AGL and (b) 2 km MSL at t = 6 h.

vector in the same direction (Fig. 13c). Nonetheless, a weaker convective banded pattern can be seen, oriented in variable directions, following both the mean wind between the surface and 5 km MSL (black arrow in Fig. 13c) and the wind shear vector (green arrow in Fig. 13c). The weak convective pattern in this simulation may be related to the fact that the low-level wind shear applied to this idealized sounding is lower than in the CTRL sounding (cf. Fig 12c). This aspect likely reduces the ability of the flow to organize into stronger and persistent convective circulations. In addition, the different directions between the low-level shear and the mean wind may be another source of disturbance, causing a reduction of convection intensity.

3) Sensitivity to atmospheric stability

Another important atmospheric factor that can influence the development of rainbands is atmospheric stability. Its impact on the development of roll-type circulations in the boundary layer has been determined in both analytical and observational studies (Kuo 1963; Weckwerth et al. 1997). However, to the authors' knowledge, the influence of static stability on orographic rainbands has been studied only in a few papers, including Kirshbaum and Durran (2005a), for shallow convection, Kirshbaum and Schultz (2018), for downwind bands and Nogueira et al. (2013), who performed a scaling analysis to evaluate the effect of small-scale terrain and upstream atmospheric conditions, including stability, on the organization of convective structures in orographic precipitation.

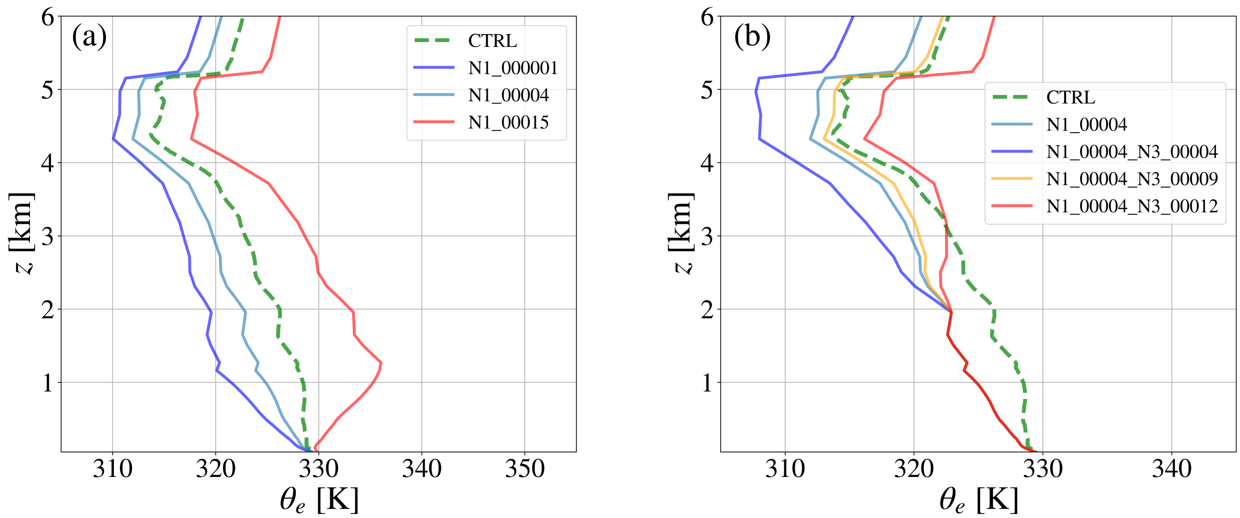

FIG. 15. Vertical profiles of equivalent potential temperature for the simulations with the modified static stability.

The dry static stability of the impinging flow has been modified by varying N and keeping the relative humidity unvaried. In particular, this sensitivity analysis is performed by varying the stability of layers 1 and 3 individually. Variations in these two layers, in fact, allow the evaluation of the effect of stability in almost the entire atmospheric profile of interest (the lowest 5 km). In particular, layer 3 describes most of the environment in which the updrafts develop, whereas layer 1 affects the evolution of thermal perturbations in the boundary layer and the buoyancy that low-level parcels gain when they are exposed to orographic uplift.

Three different simulations were performed to analyze the influence of layer 1 static stability, varying exclusively the Brunt-Väisäla frequency N_1 of the first layer (Fig. 15a). The chosen N^2 values are $N_1^2 = 0.000001$ s^{-2}, $N_1^2 = 0.00004$ s^{-2}, and $N_1^2 = 0.00015$ s^{-2}. In particular, N1_000001 describes a situation where the first layer is almost dry-neutral, with almost no convective inhibition. N1_00015 yields an opposite situation, where convective inhibition is higher (CIN = 163 J kg^{-1}) and the LFC is increased to 720 hPa. N1_00004 represents an intermediate situation, slightly more unstable in layer 1 than the CTRL sounding. Figure 15a shows that varying N_1 while keeping the relative humidity constant affects the moist static stability of the upper atmosphere, too. In fact, although N1_00015 is characterized by higher low-level stability, it exhibits stronger potential instability in the layer between 2 and 5 km MSL, where most of the convective growth processes occur. The opposite is true for N1_00004 and N1_000001, where a weaker low-level stability is associated with a less moist unstable environment in the upper layers.

The results obtained in these three simulations ~~are shown in Fig. 16.~~ The weak static stability in the boundary layer in N1_000001 makes the flow susceptible to the development of upstream convection after some hours of simulations (Figs. 16a,b). In fact, thermal perturbations in a weakly stable/neutral environment lead to the formation of amplifying circulations that can lift parcels up to their LFC, releasing the convective instability and inhibiting the organization of the banded pattern over the ridge. Thus, a combination of weak stability, weak CIN, and low LFC favors the growth of buoyant perturbations independently of the orographic uplift, inhibiting long-lived bands and favoring more cellular and disorganized convective patterns, as also highlighted by Kirshbaum and Durran (2005a) and Nogueira et al. (2013).

Conversely, N1_00015 is characterized by a sharp separation between a highly stable low-level flow and a strongly moist unstable flow aloft. This stability profile leads to the development of bands, but with a more disorganized pattern than in CTRL both at t = 6 h and t = 9 h~~, as shown in~~ Figs. 16e,f. The higher upper-level instability allows individual parcels located in this moist unstable layer to rapidly gain vertical kinetic energy and generate isolated updrafts. This process can develop independently of the orographic uplift created by the ridge, and even some kilometers upstream, disrupting the convective organization process described. Finally, a well-defined banded organization is present in N1_00004 at t = 6 h~~, as shown in~~ Fig. 16c. In this case, the banded pattern is present for several hours (until t = 8 h) and tends to become less organized later (Fig. 16d), similarly to CTRL (Fig. 6).

A further test to check the influence of upstream flow instability is performed by varying the static stability of layer 3, which comprises most of the atmospheric layer where convective updrafts develop. For this purpose, N1_00004 has been taken as reference, and the stability of layer 3 has been varied from $N_3^2 = 0.00008$ s^{-2} to $N_3^2 = 0.00004$ s^{-2} (N1_00004_N3_00004), $N_3^2 = 0.00009$ s^{-2} (N1_00004_N3_00009), and $N_3^2 = 0.00012$ s^{-2} (N1_00004_N3_00012). These experiments investigate the influence on rainband development of the amount of buoyancy gained in layer 3 by saturated air parcels. ~~The results of the simulations are shown in Fig. 17.~~ The precipitation pattern is highly disorganized in N1_00004_N3_00004, at both t = 6 h and t = 9 h (Figs. 17a,b). Convection disorganization is caused by the development of stronger vertical updrafts, with vertical

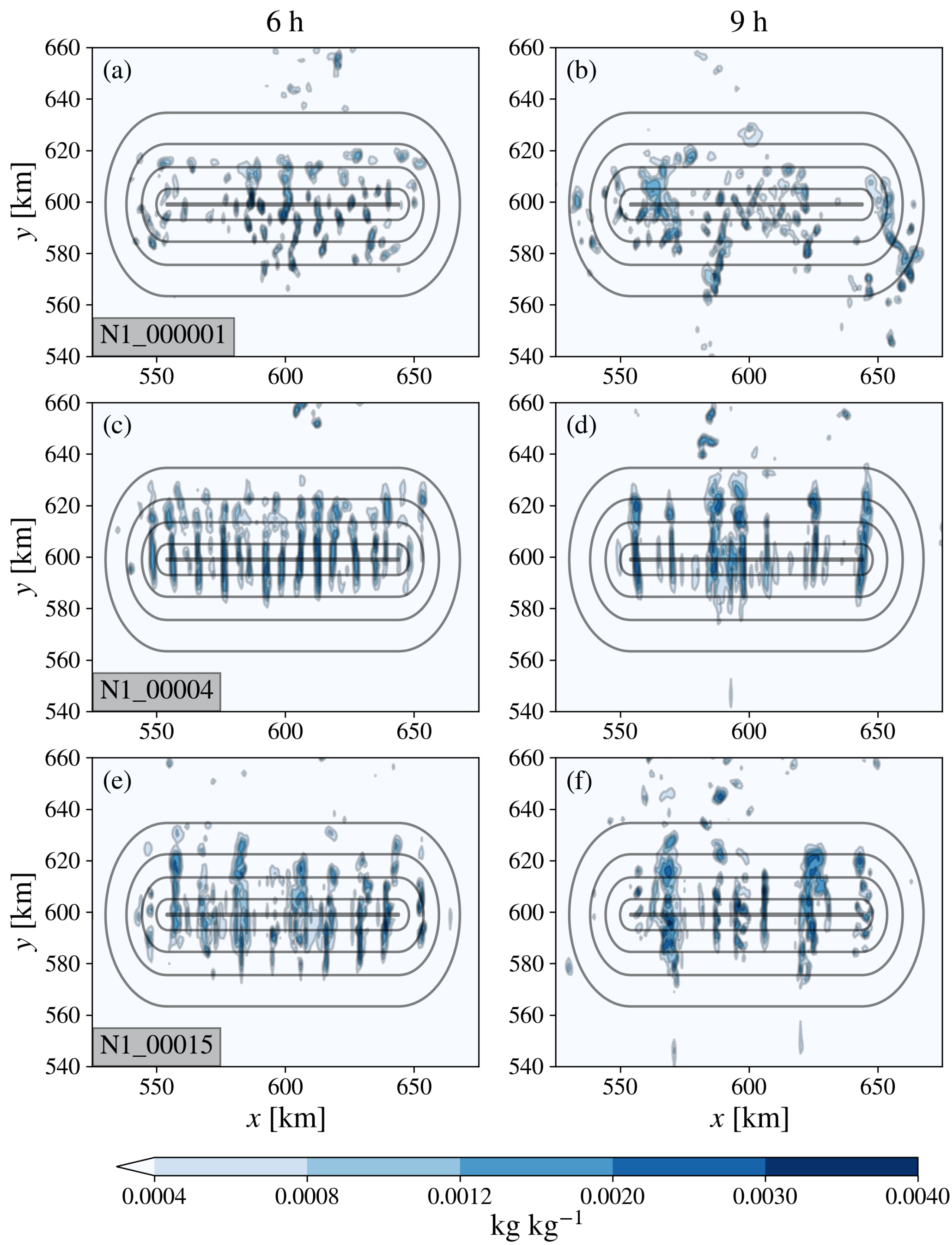

568 FIG. 16. Rain liquid mixing ratio q_r at 2 km MSL at t = 6 h (left column) and t = 9 h (right column) for (a)–(b)
569 N1_000001, (c)–(d) N1_00004, (e)–(f) N1_00015.

velocities exceeding 15 m s^{-1}, as can be seen in the y–z section in Fig. 18a. On the other hand, N1_00004_N3_00012 is associated with a background more statically stable background cloud in the upper levels. This increased stability leads to the development of weak and narrow bands at t = 6 h (Fig. 17e), associated with weak vertical velocities that can be effectively organized by the wind (Fig. 18c). Bands increase their strength at t = 9 h (Fig. 17f), conserving an ordered pattern. The smaller band spacing in N1_00004_N3_00012 may be related to the higher stability of the atmospheric layer where convective updrafts develop, consistently with Weckwerth et al. (1997), who analyzed the environmental conditions influencing the wavelength of horizontal convective rolls in Florida.

Finally, N1_00004_N3_00009 presents well-organized bands both at t = 6 h and t = 9 h. The static stability of this simulation is similar to N1_00004 (N_3^2 from 0.00008 to 0.00009), as well as the equivalent potential temperature vertical profile (Fig. 15b). However, in N1_00004_N3_00009 bands are more organized at t = 9 h than in N1_00004 (cf. Fig. 17d and Fig. 16d), demonstrating the strong sensitivity of band development and organization to the stability of the atmospheric layer where convective updrafts develop.

4) Sensitivity to relative humidity

In addition to the wind vertical profile and static stability, also the relative humidity can have an impact on the degree of organization of orographic convection. In order to test it, the relative humidity vertical profile has been varied, maintaining the dry stability of CTRL. The CTRL sounding is indeed characterized by two distinct near-saturation layers (Fig. 2), between 1 and 1.5 km and between 3 and 4 km MSL. The presence of near-saturation layers can affect the release of instability once saturation is reached in strongly potentially unstable environments. Therefore, the effect of RH on the organization of convection over the ridge has been tested by increasing and decreasing it by 5%; variations of RH were limited to the range ±5% to avoid strong changes in the moist stability vertical profile. However, for the purposes of this study, changes of 5% in RH are sufficient to draw solid conclusions about the effect of RH on the degree of convective organization. In detail, RH_INCR5 and RH_RED5 are characterized respectively by a RH profile increased and decreased by 5% throughout all the atmospheric layer in comparison with CTRL (Fig. 19a). Differently, RH_INCR5_LL is characterized by an increase of 5% in RH below 2.6

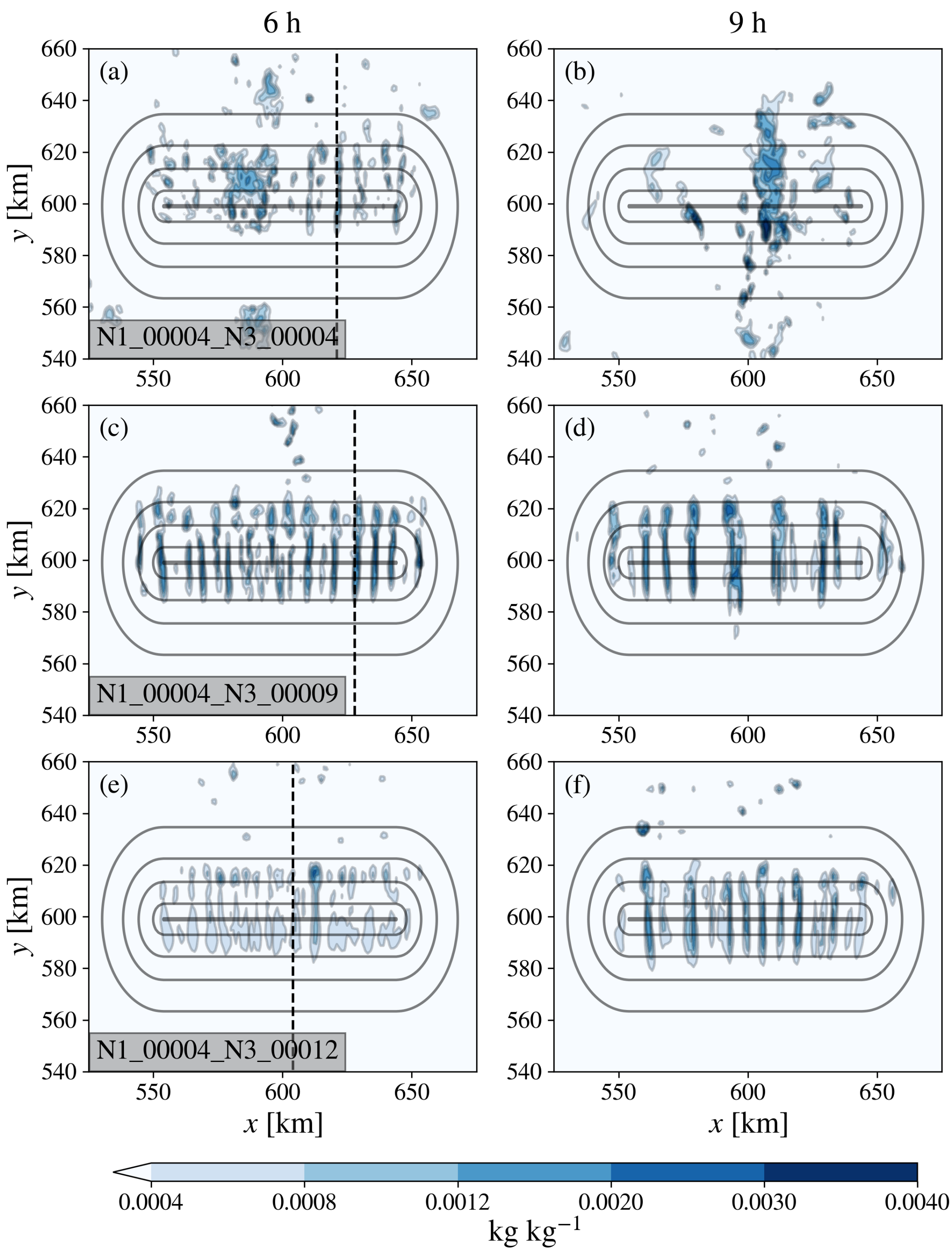

FIG. 17. Rain liquid mixing ratio q_r at 2 km MSL at t = 6 h (left column) and t = 9 h (right column) for (a)–(b) N1_00004_N3_00004, (c)–(d) N1_00004_N3_00009, (e)–(f) N1_00004_N3_00012. The dashed lines in (a), (c), and (e) represent the location of the y–z sections shown in Fig. 18.

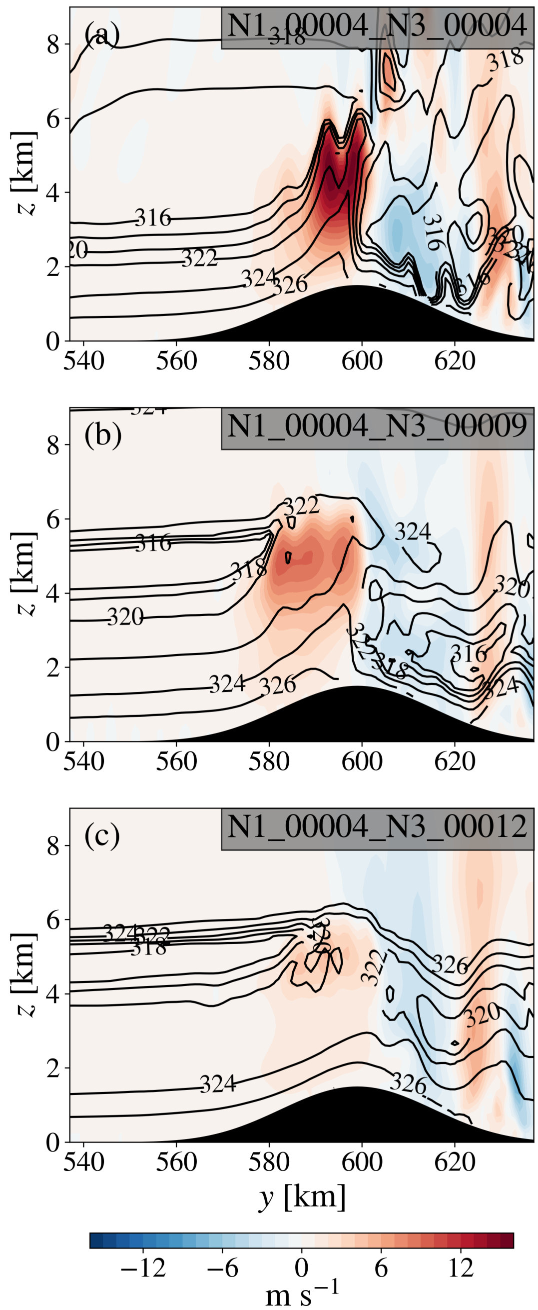

616 Fig. 18. South–north (y–z) cross sections showing equivalent potential temperature θ_e (contours) and vertical wind velocity w (shading) at t = 6 h, for (a) N1_00004_N3_00004 at x = 623, (b) N1_00004_N3_00009 at x = 630, (c) N1_00004_N3_00012 at x = 605.

km and above 4.2 km MSL compared to CTRL, whereas in RH_INCR5_UL the 5% increase in RH with respect to CTRL is applied only above 2.3 km MSL (Fig. 19b). The aim of the last two

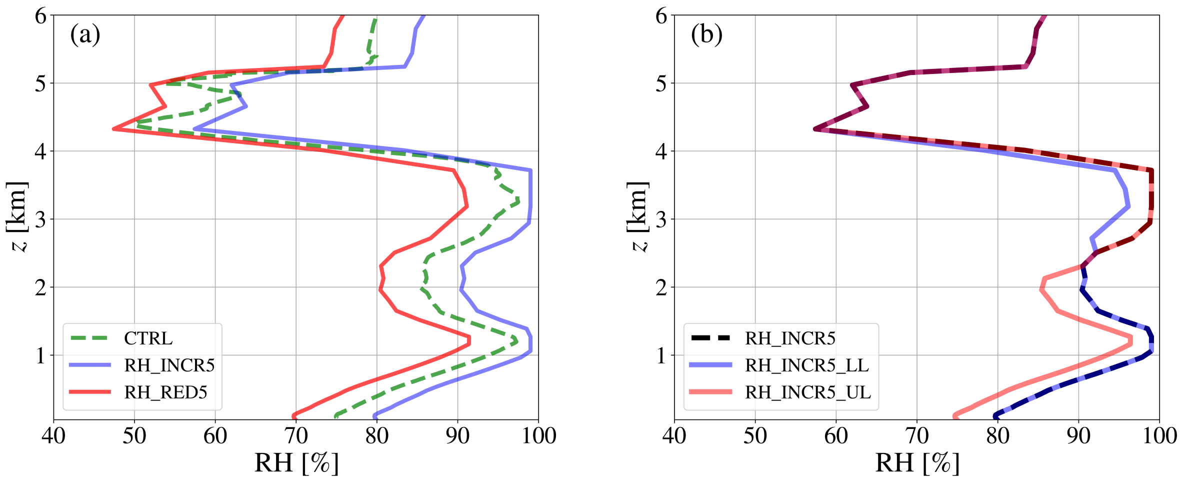

FIG. 19. Relative humidity vertical profiles in the lowest 6 km for the sensitivity simulations to RH and for CTRL.

simulations is to analyze separately the effect of the two near-saturation layers that characterize the CTRL sounding. In all the above-mentioned vertical profiles, the maximum RH was fixed to 99%.

The comparison of rain liquid mixing ratio patterns in Fig. 20a,b and 20c,d shows completely different band organization between RH_RED5 and RH_INCR5. The model simulates a banded pattern even with a reduction of RH throughout all the atmospheric column, both at t = 6 h and t = 9 h. In fact, the LFC corresponding to the sounding of this simulation is higher than in the CTRL sounding and low-level parcels do not immediately gain buoyancy as they are lifted. Moreover, a stronger convective inhibition (CIN = 52 J kg^{-1}) preserves a band-shaped convective pattern over the ridge for many hours and no spurious convection occurs far from the mountain. On the other hand, an increase of RH leads to a complete disorganization of the convective pattern and favors the development of convection far from the ridge starting from the fourth hour of simulation. The susceptibility to convection far from the ridge is enhanced in this simulation even if the dry static stability of RH_INCR5 is strictly close to that of CTRL. The reason for this behavior is revealed by the results of the other two simulations. An increase in low-level moisture and the resulting presence of a saturated layer between 1000 and 1500 m does not preclude a banded precipitation pattern (Fig. 20e,f). The simulated orographic rainbands are more intense and characterized by a narrower spacing, and they persist at t = 9 h. The narrower spacing of the rainbands when the low-level RH is increased is consistent with Kirshbaum et al. (2007a), who highlighted narrower band spacing when the cloud base is lower. In RH_INCR5_UL (Fig. 20g,h) the convective pattern

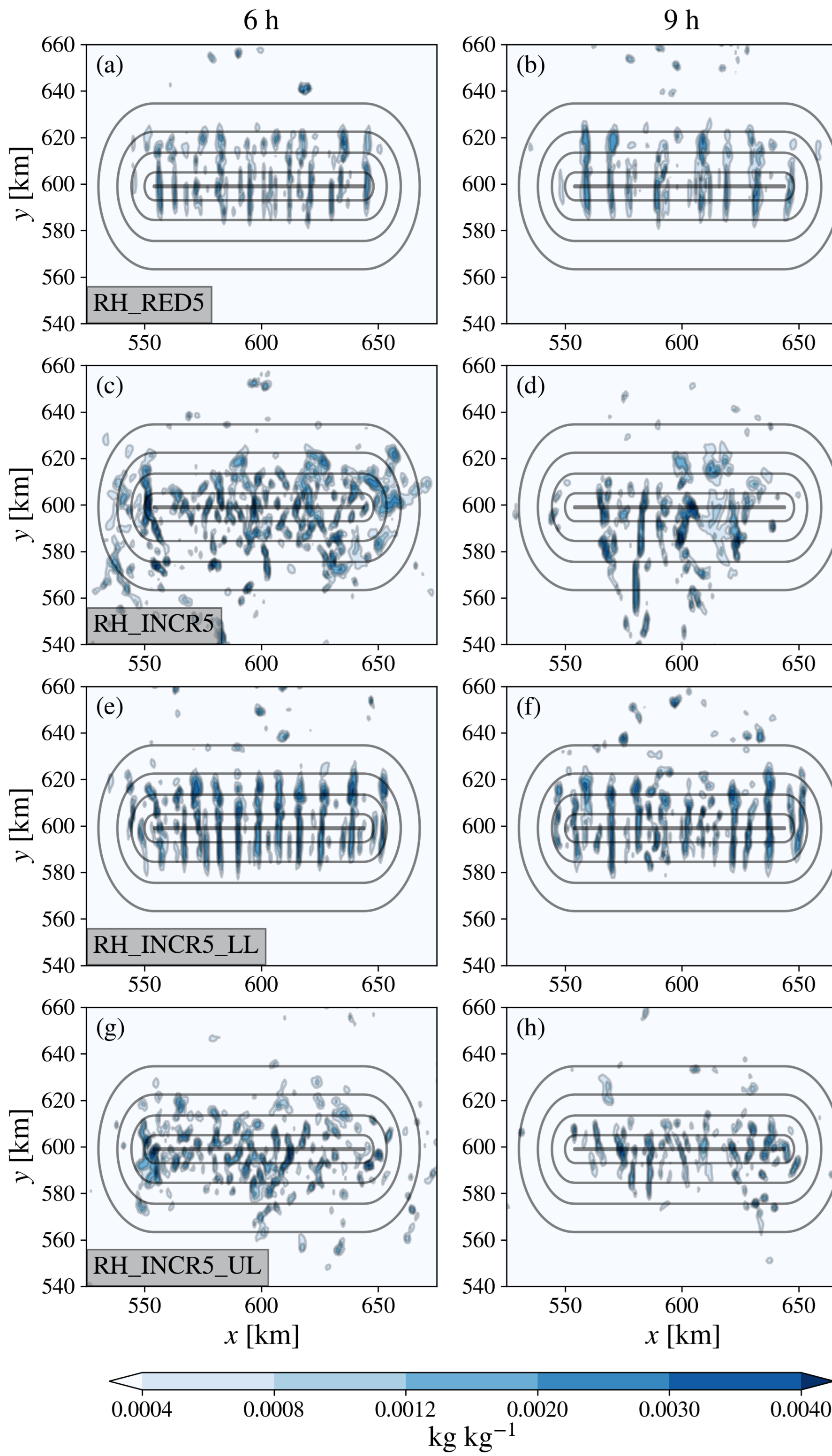

637 FIG. 20. Rain liquid mixing ratio q_r at 2 km MSL at t = 6 h (left column) and t = 9 h (right column) for (a)–(b)
638 RH_RED5, (c)–(d) RH_INCR5, (e)–(f) RH_INCR5_LL, (g)–(h) RH_INCR5_UL.

is instead more cellular and messy. The results of these simulations suggest that near-saturated mid-level layers are a source of convective disorganization in moist, potentially unstable flows encountering a ridge. The mechanism causing this disorganization is similar to that of N1_00015 shown in the previous section. The presence of a near-saturated layer at mid-troposphere allows parcels to condense also with small vertical velocity perturbations, thus explaining the development of convection also upstream of the ridge, which completely inhibits the organization of orographic rainbands.

6. Conclusions

Deep orographic rainbands that developed in the last stages of the Vaia storm over the eastern Italian Alps have been taken as a pretext to conduct different sensitivity tests to study their formation and development by means of idealized numerical simulations with the WRF model, using a simplified smoothed topographic profile loosely representative of the Alpine ridge. The simulations have been performed maintaining initial environmental conditions similar to those observed during the Vaia storm, capable of causing rainfall intensities up to 60 mm h^{-1}. Variations of the upstream sounding have been employed to evaluate the influence of wind speed and direction, vertical wind shear, vertical stability profile and relative humidity on band development, persistence and structure.

A sensitivity analysis on model resolution, using simulations with horizontal grid spacing of 200, 500 and 1000 m, highlighted consistent results in terms of band spacing and width. This aspect was quantitatively evaluated by means of a Fourier analysis of the one-hour accumulated rainfall amounts, confirming that, in this case, a grid spacing of 1000 m is sufficient to capture the main features of the orographic rainbands.

Results from a simulation with a slightly simplified sounding with respect to the observed one showed that rainbands appear as horizontal roll-like circulations with precipitations generated by the tilted updrafts, resembling the typical characteristics highlighted in previous studies (e.g., Kirshbaum and Durran 2005a; Fuhrer and Schär 2007). However, in the present case, characterized by deeper convection, updrafts reach a higher altitude, up to 6–7 km MSL. Bands vary their position in time, distributing precipitation rather evenly over the ridge.

The sensitivity to wind speed highlighted that, in the absence of vertical wind shear, convection is generally more cellular, with less organized rainbands. This result is in agreement with previous findings (e.g., Asai 1970; Yoshizaki et al. 2000; Kirshbaum and Durran 2005a; Fuhrer and Schär 2007), as wind shear breaks the local isotropy of convection and favors the growth of horizontal roll vortices oriented in its direction. However, weakly organized bands developed even in simulations with vertically-constant approaching wind, provided that wind speed is sufficiently intense to guarantee a flow-over regime, because the interaction with the ridge generates a weak wind shear in the low levels, partly favoring band development. A rotation of the wind with height, instead, disadvantages band formation and persistence, especially if the wind shear vector varies its direction with altitude. An impinging flow with unidirectional wind shear, instead, can sustain the development of rainbands. Nevertheless, their weak intensity confirms that the most favorable condition for orographic rainband development is the alignment of wind shear and wind vectors.

The sensitivity analysis to atmospheric stability revealed that a nearly dry neutral layer in the low levels, with almost no convective inhibition, favors the development of cellular convection upstream of the ridge independently of the orographic uplift, not allowing the subsequent rainband formation over the ridge. Thus, a certain amount of convective inhibition is needed at low levels. For example, a CIN of 43 J Kg^{-1} in the original sounding allowed the formation of well-developed and long-lived rainbands over the ridge. Apart from that, bands are capable of generating within a rather wide range of low-level static stability values if the upper atmospheric layers are moist statically unstable. Nevertheless, strongly moist unstable atmospheric stratification in the upper layers, where convection develops, causes a disorganization of the banded precipitation pattern. The rainband disorganization can be caused by isolated upper-level convection, even upstream of the ridge, or by too intense updrafts over the ridge, with a rapid release of instability in the highly unstable saturated layers. Isolated upper-level convection in strongly moist unstable layers can occur even when the lower layer is stable, as in N1_00015, whereas strong updrafts over the ridge are favored with low-level moist instability, as in N1_00004_N3_00004. Strong updrafts imply a rapid convective growth rate, which does not let the wind shear and the intense wind speed tilt the updrafts (Miglietta and Rotunno 2009).

Similarly, sensitivity to the relative humidity profile showed that near-saturation layers located between 3 and 4 km MSL in the presence of moist instability disrupt the convective organization.

In this case, individual updrafts develop starting from this near-saturated layer independently of the convective initiation process generated by the orographic uplift of the flow induced by the ridge. Without the presence of such a layer, relative humidity does not have a strong impact on rainbands, even if, as expected, their intensity grows with increasing low-level relative humidity.

This work has analyzed atmospheric factors affecting the development of intense orographic rainbands, extending the findings of previous studies focusing on shallow convection and using more realistic and complex vertical soundings. The results confirmed that, also with these thermodynamic conditions, the development of orographic rainbands is mainly favored with a unidirectional sheared flow when the release of instability is confined over the orography by the presence of sufficient dry static stability in the lowest layers and not excessive moist instability in the upper levels, where the updrafts develop. Moreover, the present work also highlighted that near-saturation in this layer disrupts convective organization due to the development of individual updrafts not connected to orographic lifting, pointing out the importance of the correct simulation of RH in this layer for capturing convective rainbands. However, the results showed that deep banded orographic convection, with different degrees of organization, can develop over a rather wide range of perturbations of the original sounding, confirming that rainbands are not an unusual feature of fall storms over the Italian Alps and remarking the importance of improving the forecasting capabilities of these phenomena, often associated with extreme precipitation.

Acknowledgments. The Authors are grateful to Prof. David M. Schultz and two anonymous Reviewers for providing constructive reviews and useful suggestions to improve the quality of the article. The Authors are grateful to the Italian Civil Protection Department for providing radar images and to the Italian National Center for Aeronautical Meteorology and Climatology of the Italian Air Force for high-resolution data from radiosoundings at Udine-Rivolto. MMM acknowledges financial support from Next Generation EU, Mission 4, Component 1, CUP B53D23007360006, project "Thunderstorm outflows measurements and modeling for strong WIND nowcast and RISK mitigation (WIND RISK)". SD acknowledges financial support from Next Generation EU, Mission 4, Component 1, CUP B53D23007490006, project "Exploring Atmospheric Rivers in the Mediterranean and their connection with extreme hydrometeorological events over Italy: observation, modelling and impacts (ARMEX)"

Data availability statement. The numerical model simulations upon which this study is based are too large to archive. However, simulations output can be provided by the authors upon request, as well as all the information needed to replicate the simulations. Input soundings of the simulations and Python scripts for plotting the results are archived at https://github.com/TullioDegiacomi/Degiacomi_et_al_2024. The WRF model (version 4.1.2) was downloaded from https://github.com/wrf-model/.

References

Anquetin, S., F. Minsicloux, J.-D. Creutin, and S. Cosma, 2003: Numerical simulation of orographic rainbands. *Journal of Geophysical Research: Atmospheres*, **108 (D8)**, https://doi.org/https://doi.org/10.1029/2002JD001593.

Asai, T., 1970: Stability of a plane parallel flow with variable vertical shear and unstable stratification. *Journal of the Meteorological Society of Japan. Ser. II*, **48 (2)**, 129–139, https://doi.org/DOI:10.2151/JMSJ1965.48.2_129.

Barrett, A. I., S. L. Gray, D. J. Kirshbaum, N. M. Roberts, D. M. Schultz, and J. G. Fairman, 2016: The utility of convection-permitting ensembles for the prediction of stationary convective bands. *Monthly Weather Review*, **144 (3)**, 1093 – 1114, https://doi.org/10.1175/MWR-D-15-0148.1.

Barrett, A. I., S. L. Gray, D. J. Kirshbaum, N. M. Roberts, D. M. Schultz, and J. G. Fairman Jr, 2015: Synoptic versus orographic control on stationary convective banding. *Quarterly Journal of the Royal Meteorological Society*, **141 (689)**, 1101–1113, https://doi.org/https://doi.org/10.1002/qj.2409.

Borga, M., P. Boscolo, F. Zanon, and M. Sangati, 2007: Hydrometeorological analysis of the 29 august 2003 flash flood in the eastern italian alps. *Journal of Hydrometeorology*, **8 (5)**, 1049 – 1067, https://doi.org/https://doi.org/10.1175/JHM593.1.

Bougeault, P., and Coauthors, 2001: The map special observing period. *Bulletin of the American Meteorological Society*, **82 (3)**, 433 – 462, https://doi.org/10.1175/1520-0477(2001)082<0433:TMSOP>2.3.CO;2.

Cavaleri, L., and Coauthors, 2019: The october 29, 2018 storm in northern italy – an exceptional event and its modeling. *Progress in Oceanography*, **178**, 102 178, https://doi.org/https://doi.org/10.1016/j.pocean.2019.102178.

Chen, S.-H., and Y.-L. Lin, 2004: Orographic effects on a conditionally unstable flow over an idealized three-dimensional mesoscale mountain. *Meteorology and Atmospheric Physics*, **88**, 1–21, https://doi.org/https://doi.org/10.1007/s00703-003-0047-6.

Cosma, S., E. Richard, and F. Miniscloux, 2002: The role of small-scale orographic features in the spatial distribution of precipitation. *Quarterly Journal of the Royal Meteorological Society*, **128 (579)**, 75–92, https://doi.org/https://doi.org/10.1256/00359000260498798.

Davolio, S., S. Della Fera, S. Laviola, M. Miglietta, and V. Levizzani, 2020: Heavy precipitation over italy from the mediterranean storm “vaia” in october 2018: Assessing the role of an atmospheric river. *Monthly Weather Review*, **148**, 3571–3588, https://doi.org/10.1175/MWR-D-20-0021.1.

Davolio, S., A. Volonté, A. Manzato, A. Pucillo, A. Cicogna, and M. E. Ferrario, 2016: Mechanisms producing different precipitation patterns over north-eastern italy: insights from hymex-sop1 and previous events. *Quarterly Journal of the Royal Meteorological Society*, **142 (S1)**, 188–205, https://doi.org/https://doi.org/10.1002/qj.2731.

Ducrocq, V., and Coauthors, 2014: Hymex-sop1: The field campaign dedicated to heavy precipitation and flash flooding in the northwestern mediterranean. *Bulletin of the American Meteorological Society*, **95 (7)**, 1083 – 1100, https://doi.org/10.1175/BAMS-D-12-00244.1.

Dudhia, J., 1989: Numerical study of convection observed during the winter monsoon experiment using a mesoscale two-dimensional model. *Journal of The Atmospheric Sciences - J ATMOS SCI*, **46**, 3077–3107, https://doi.org/10.1175/1520-0469(1989)046<3077:NSOCOD>2.0.CO;2.

Ferretti, R., and Coauthors, 2014: Overview of the first hymex special observation period over italy: observations and model results. *Hydrology and Earth System Sciences*, **18 (5)**, 1953–1977, https://doi.org/10.5194/hess-18-1953-2014.

Fuhrer, O., and C. Schär, 2007: Dynamics of orographically triggered banded convection in sheared moist orographic flows. *Journal of the Atmospheric Sciences*, **64 (10)**, 3542 – 3561, https://doi.org/10.1175/JAS4024.1.

Galewsky, J., 2008: Orographic clouds in terrain-blocked flows: An idealized modeling study. *Journal of the Atmospheric Sciences*, **65 (11)**, 3460 – 3478, https://doi.org/10.1175/2008JAS2435.1.

Giovannini, L., S. Davolio, M. Zaramella, D. Zardi, and M. Borga, 2021: Multi-model convection-resolving simulations of the october 2018 vaia storm over northeastern italy. *Atmospheric Research*, **253**, 105 455, https://doi.org/https://doi.org/10.1016/j.atmosres.2021.105455.

Godart, A., S. Anquetin, and E. Leblois, 2009: Rainfall regimes associated with banded convection in the cévennes-vivarais area. *Meteorology and atmospheric physics*, **103 (1)**, 25–34, https://doi.org/https://doi.org/10.1007/s00703-008-0326-3.

Hong, S. Y., and J.-O. J. Lim, 2006: The wrf single-moment 6-class microphysics scheme (wsm6). *Asia-pacific Journal of Atmospheric Sciences*, **42**, 129–151.

Hong, S.-Y., Y. Noh, and J. Dudhia, 2006: A new vertical diffusion package with an explicit treatment of entrainment processes. *Monthly Weather Review - MON WEATHER REV*, **134**, https://doi.org/10.1175/MWR3199.1.

Jiménez, P. A., J. Dudhia, J. F. González-Rouco, J. Navarro, J. P. Montávez, and E. García-Bustamante, 2012: A revised scheme for the wrf surface layer formulation. *Monthly Weather Review*, **140 (3)**, 898 – 918, https://doi.org/10.1175/MWR-D-11-00056.1.

Kirshbaum, D., R. Rotunno, and G. Bryan, 2007a: The spacing of orographic rainbands triggered by small-scale topography. *J. Atmos. Sci.*, **64**, https://doi.org/10.1175/2007JAS2335.1.

Kirshbaum, D. J., G. H. Bryan, R. Rotunno, and D. R. Durran, 2007b: The triggering of orographic rainbands by small-scale topography. *Journal of the Atmospheric Sciences*, **64 (5)**, 1530 – 1549, https://doi.org/10.1175/JAS3924.1.

Kirshbaum, D. J., and D. R. Durran, 2005a: Atmospheric factors governing banded orographic convection. *Journal of the Atmospheric Sciences*, **62 (10)**, 3758 – 3774, https://doi.org/10.1175/JAS3568.1.

Kirshbaum, D. J., and D. R. Durran, 2005b: Observations and modeling of banded orographic convection. *Journal of the Atmospheric Sciences*, **62 (5)**, 1463 – 1479, https://doi.org/10.1175/JAS3417.1.

Kirshbaum, D. J., and D. M. Schultz, 2018: Convective cloud bands downwind of mesoscale mountain ridges. *Journal of the Atmospheric Sciences*, **75 (12)**, 4265 – 4286, https://doi.org/10.1175/JAS-D-18-0211.1.

Kuo, H., 1963: Perturbations of plane couette flow in stratified fluid and origin of cloud streets. *The Physics of Fluids*, **6 (2)**, 195–211, https://doi.org/https://doi.org/10.1063/1.1706719.

Li, S., S. Jaroszynski, S. Pearse, L. Orf, and J. Clyne, 2019: Vapor: A visualization package tailored to analyze simulation data in earth system science. *Atmosphere*, **10 (9)**, https://doi.org/10.3390/atmos10090488.

Manzato, A., S. Davolio, M. M. Miglietta, A. Pucillo, and M. Setvák, 2015: 12 september 2012: A supercell outbreak in ne italy? *Atmospheric Research*, **153**, 98–118, https://doi.org/https://doi.org/10.1016/j.atmosres.2014.07.019.

Medina, S., and R. A. Houze, 2003: Air motions and precipitation growth in alpine storms. *Quarterly Journal of the Royal Meteorological Society*, **129 (588)**, 345–371, https://doi.org/https://doi.org/10.1256/qj.02.13.

Miglietta, M. M., and S. Davolio, 2022: Dynamical forcings in heavy precipitation events over italy: lessons from the hymex sop1 campaign. *Hydrology and Earth System Sciences*, **26 (3)**, 627–646, https://doi.org/10.5194/hess-26-627-2022.

Miglietta, M. M., A. Manzato, and R. Rotunno, 2016: Characteristics and predictability of a supercell during hymex sop1. *Quarterly Journal of the Royal Meteorological Society*, **142 (700)**, 2839–2853, https://doi.org/https://doi.org/10.1002/qj.2872.

Miglietta, M. M., and R. Rotunno, 2009: Numerical simulations of conditionally unstable flows over a mountain ridge. *Journal of the Atmospheric Sciences*, **66 (7)**, 1865 – 1885, https://doi.org/10.1175/2009JAS2902.1.

Miller, D. K., 2012: Near-term effects of the lower atmosphere in simulated northwest flow snowfall forced over the southern appalachians. *Weather and Forecasting*, **27 (5)**, 1198 – 1216, https://doi.org/10.1175/WAF-D-11-00103.1.

Miniscloux, F., J. Creutin, and S. Anquetin, 2001: Geostatistical analysis of orographic rainbands. *Journal of Applied Meteorology - J APPL METEOROL*, **40**, 1835–1854, https://doi.org/10.1175/1520-0450(2001)040<1835:GAOOR>2.0.CO;2.

Mlawer, E. J., S. J. Taubman, P. D. Brown, M. J. Iacono, and S. A. Clough, 1997: Radiative transfer for inhomogeneous atmospheres: Rrtm, a validated correlated-k model for the longwave. *Journal of Geophysical Research: Atmospheres*, **102 (D14)**, 16 663–16 682, https://doi.org/https://doi.org/10.1029/97JD00237.

Nogueira, M., A. P. Barros, and P. M. A. Miranda, 2013: Multifractal properties of embedded convective structures in orographic precipitation: toward subgrid-scale predictability. *Nonlinear Processes in Geophysics*, **20 (5)**, 605–620, https://doi.org/10.5194/npg-20-605-2013.

Peng, M. S., S.-W. Li, S. W. Chang, and R. T. Williams, 1995: Flow over mountains: Coriolis force, transient troughs and three dimensionality. *Quarterly Journal of the Royal Meteorological Society*, **121 (523)**, 593–613, https://doi.org/https://doi.org/10.1002/qj.49712152307.

Ricchi, A., D. Bonaldo, G. Cioni, S. Carniel, and M. M. Miglietta, 2021: Simulation of a flash-flood event over the adriatic sea with a high-resolution atmosphere-ocean–wave coupled system. *Scientific Reports*, **11 (9388)**, https://doi.org/https://doi.org/10.1038/s41598-021-88476-1.

Rotunno, R., and R. A. Houze, 2007: Lessons on orographic precipitation from the mesoscale alpine programme. *Quarterly Journal of the Royal Meteorological Society*, **133 (625)**, 811–830, https://doi.org/https://doi.org/10.1002/qj.67.

Schneider, L., C. Barthlott, A. I. Barrett, and C. Hoose, 2018: The precipitation response to variable terrain forcing over low mountain ranges in different weather regimes. *Quarterly Journal of the Royal Meteorological Society*, **144 (713)**, 970–989, https://doi.org/https://doi.org/10.1002/qj.3250.

Schneidereit, M., and C. Schär, 2000: Idealised numerical experiments of alpine flow regimes and southside precipitation events. *Meteorology and Atmospheric Physics*, **72**, 233–250, https://doi.org/https://doi.org/10.1007/s007030050018.

Schumacher, R. S., D. M. Schultz, and J. A. Knox, 2010: Convective snowbands downstream of the rocky mountains in an environment with conditional, dry symmetric, and inertial instabilities. *Monthly Weather Review*, **138 (12)**, 4416 – 4438, https://doi.org/10.1175/2010MWR3334.1.

Schumacher, R. S., D. M. Schultz, and J. A. Knox, 2015: Influence of terrain resolution on banded convection in the lee of the rocky mountains. *Monthly Weather Review*, **143 (4)**, 1399 – 1416, https://doi.org/10.1175/MWR-D-14-00255.1.

Siedersleben, S. K., and A. Gohm, 2016: The missing link between terrain-induced potential vorticity banners and banded convection. *Monthly Weather Review*, **144 (11)**, 4063 – 4080, https://doi.org/10.1175/MWR-D-16-0042.1.

Skamarock et al., W., 2019: A description of the advanced research wrf version 3. https://doi.org/doi:10.5065/D68S4MVH.

Smith, R. B., 1988: Linear theory of stratified flow past an isolated mountain in isosteric coordinates. *Journal of the atmospheric sciences*, **45 (24)**, 3889–3896, https://doi.org/10.1175/1520-0469(1988)045<3889:LTOSFP>2.0.CO;2.

Stocchi, P., and S. Davolio, 2017: Intense air-sea exchanges and heavy orographic precipitation over italy: The role of adriatic sea surface temperature uncertainty. *Atmospheric Research*, **196**, 62–82, https://doi.org/https://doi.org/10.1016/j.atmosres.2017.06.004.

Visualization & Analysis Systems Technologies, 2023: Visualization and analysis platform for ocean, atmosphere, and solar researchers (vapor). Boulder, CO: UCAR/NCAR - Computational and Information System Lab, https://doi.org/doi:10.5281/zenodo.7779648.

Weckwerth, T. M., J. W. Wilson, R. M. Wakimoto, and N. A. Crook, 1997: Horizontal convective rolls: Determining the environmental conditions supporting their existence and characteristics. *Monthly Weather Review*, **125 (4)**, 505 – 526, https://doi.org/10.1175/1520-0493(1997)125<0505:HCRDTE>2.0.CO;2.

Yang et al., Z.-L., 2011: The community Noah land surface model with multiparameterization options (Noah-MP): 2. Evaluation over global river basins. *Journal of Geophysical Research*, **116**, 12 110, https://doi.org/10.1029/2010JD015140.

Yoshizaki, M., and Coauthors, 2000: Analytical and numerical study of the 26 june 1998 orographic rainband observed in western kyushu, japan. *Journal of the Meteorological Society of Japan. Ser. II*, **78 (6)**, 835–856, https://doi.org/10.2151/jmsj1965.78.6_835.